Journal of Electroanalytical Chemistry 651 (2011) 80–93

Contents lists available at ScienceDirect

Journal of Electroanalytical Chemistry

journal homepage: www.elsevier.com/locate/jelechem

Evaluation of the intrinsic kinetic activity of nanoparticle ensembles under steady-state conditions

Cynthia G. Zoski *, José L. Fernández [1], Kasun Imaduwage, Dulan Gunasekara, Raghuveer Vadari

Department of Chemistry and Biochemistry, New Mexico State University, MSC 3C, Las Cruces, NM 88003, United States

ARTICLE INFO

Article history:
Received 27 July 2010
Received in revised form 15 October 2010
Accepted 25 October 2010
Available online 30 October 2010

Keywords:
Pt nanoparticles
Intrinsic kinetic activity
Nanoparticle ensembles
Steady-state voltammograms
Reverse microemulsion

ABSTRACT

We report theory and strategies for evaluating the intrinsic kinetic activity for oxygen reduction at Pt nanoparticle (NP) ensembles on a large glassy carbon electrode (GCE) under steady-state conditions. Pt NPs were synthesized using reverse microemulsions which facilitated the deposition of random ensembles of bare NPs with controlled NP mean size and coverage. Steady-state voltammograms (SSVs) for oxygen reduction were recorded for various NP ensembles with different NP size and coverage. The effects of NP coverage and mass-transport rate on SSV features were analyzed. For SSVs normalized with respect to their limiting current, more negative potentials are needed to reach the limiting current region and the *i–E* slope decreases as NP coverage decreases. For those normalized SSVs having unequal limiting currents, the kinetic rate relative to the mass-transport rate changes and plays a role in the decreasing steepness of the SSV. In contrast, normalized SSVs recorded under the same mass transport conditions and decreasing NP coverage are displaced negatively along the potential axis without a change in the *i–E* slope. Normalized SSVs recorded using the same mass transport conditions on electrodes with similar fractions of inactive area but different NP sizes were found to be similar. Tafel plots were constructed by processing the SSVs either directly through the use of the electroactive surface area A_{ES} or indirectly through a two-step procedure that uses the geometric surface area where an apparent potential-dependent kinetic current density $j_K^{app}(E)$ is first calculated. These two approaches are equivalent and the resulting kinetic current density $j_K(E)$ dependencies were shown to be equivalent. The direct method is applicable when A_{ES} can be determined whereas the indirect approach is useful when the measurement of A_{EAS} is not possible, but information relating to the fraction of active or inactive area is available.

1. Introduction

The nanoscale design of electrocatalysts continues to be of great interest due to the need to limit the quantity of noble metals used in renewable energy devices such as fuel cells while still supporting facile mass and charge transport [1–3]. In PEM fuel cells, for example, strategies to minimize the Pt content have included decreasing the nanoparticle (NP) size and/or the loading of NP dispersions. Such strategies involve supported metal NPs and have led to fundamental questions regarding the effect of NP size and spacing in general on electrocatalytic reactions [4–20]. In particular, the O_2 reduction reaction has been studied on Pt in various forms including polycrystalline [21,22], single crystal [23–27], single NPs [28] and dispersions [4–6,8–11,15,16,29–31] on carbon supports, and with NP arrays [19,32] and ensembles [33–35]. Other electrocatalytic reactions such as formic acid oxidation has been studied on Pt electrodeposited on a glassy carbon support [20], carbon monoxide oxidation at Pt NP dispersions on a Au support [36] as well as at Au NP ensembles [37–39], and methanol oxidation on porous nanostructured Pt [40].

Pt NP ensembles and arrays have been made using a variety of methods including dip-coating glassy carbon electrodes (GCE) with poly(diallyldimethylammonium)chloride (PDDA) followed by immersion into Pt NP solution [34], using block co-polymers and Pt-salt solutions followed by Ar plasma treatment to reduce the metal salt and remove the polymer template [32,41,42], immobilizing Pt dendrimer-encapsulated NPs on GCEs [33,35], immobilization of Pt NPs prepared by reverse microemulsions [43–45], by electron beam lithography [19], pulsed-laser deposition [46], ultra-high vacuum deposition [47], and colloidal lithography [48].

Investigations involving kinetics associated with electrocatalytic reactions at NP-covered surfaces have been carried out using rotating disk voltammetry, a steady-state technique involving primarily convective mass transport with diffusion occurring within the convection layer, or transient techniques such as cyclic voltammetry which involve mass transport by diffusion only. In rotating

* Corresponding author. Tel.: +1 575 646 5292.
E-mail addresses: czoski@nmsu.edu (C.G. Zoski), jlfernan@fiq.unl.edu.ar (J.L. Fernández).
[1] Present address: Facultad de Ingeniería Química, Universidad Nacional del Litoral, Santiago del Estero 2829, 3000 Santa Fe, Argentina.

1572-6657/$ - see front matter © 2010 Elsevier B.V. All rights reserved.
doi:10.1016/j.jelechem.2010.10.023

Nomenclature

Abbreviations

CV	cyclic voltammogram, cyclic voltammetry
GCE	glassy carbon electrode
NP	nanoparticle
NP/GCE	nanoparticle modified glassy carbon electrode
NP RME	nanoparticle reverse microemulsion
RME	reverse microemulsion
SCE	saturated calomel reference electrode
SEM	scanning electron microscopy
SECM	scanning electrochemical microscopy
SHE	standard hydrogen electrode
SSV	steady-state voltammogram, steady-state voltammetry
TEM	transmission electron microscopy
UME	ultramicroelectrode

Symbols

A_{ES}	electroactive surface area
A_{GS}	geometric surface area
D_O	diffusion coefficient
d_{CV}	characteristic diffusion length of a cyclic voltammetric experiment
d_{ss}	steady-state diffusion length around a supported nanoparticle
E	potential
I	dimensionless steady-state current
i	steady-state current
i_L	steady-state limiting current
$i_{L,C}$	steady-state limiting current due to convection
i_K	steady-state current due to kinetics
$i_{L,NP}$	steady-state limiting current due to diffusion to supported nanoparticles
j_K	intrinsic kinetic steady-state current density
j_K^{app}	apparent kinetic steady-state current density
j_L	limiting steady-state current density
j_o	exchange current density
m_C	mass transfer coefficient due to convection
m_{NP}	mass transfer coefficient due to diffusion to supported nanoparticles
m'_{NP}	collective diffusive mass transport coefficient to a nanoparticle modified supporting electrode
p	number of nanoparticles or circular zones
R_D	radius of the supporting circular inlaid disk electrode
r_{NP}	radius of a spherical nanoparticle
R_0	radius of the circular inactive zone around a spherical nanoparticle in a uniform array of nanoparticles used in describing nanoparticle separation
R_0^{ran}	designates a random distribution of nanoparticle separations
$R_0^{ran,avg}$	average NP spacing in a random array of R_0^{ran} circular zones
t_{CV}	characteristic time of a cyclic voltammetric experiment
t_{ss}	time required for the steady-state diffusion length to be established
v	sweep rate of a CV experiment
$V_{NP\ RME}$	volume of NP RME deposited on a GCE surface
$W\#$	the molecular water-to-surfactant ratio used in RME syntheses to approximate the size of NP to be made. $W2$, $W10$, and $W30$ were used in these studies
γ	related to the geometry of an active site (= 1 for nanodisk; = 2 for nanohemisphere; = 4 for spherical nanoparticle)
δ_C	magnitude of the solution diffusion layer due to convection
θ	fraction of geometric surface area that is inactive
$1-\theta$	fraction of geometric surface area that is active
ρ_{NP}	nanoparticle density on the supporting electrode

disk experiments [8,15,16,30,35,49], kinetic behavior is evaluated using Koutecky–Levich and/or Tafel plots with the assumption that the electrode surface has a uniform monolayer of NPs so that diffusion within the convection layer remains linear. When a monolayer of NPs cannot be assumed, the Koutecky–Levich equation must be modified to reflect non-linear diffusion to the NPs within the convection layer so that the description of electrode area becomes important (i.e. geometric area vs. electrochemical active area) [18,50,51]. This is similar to the modification of the Koutecky–Levich equation for an electrode covered with thin films such as Nafion or conductive polymers [52–62]. In contrast, investigations involving ensembles of NPs on large geometric area electrodes have primarily been carried out under time-dependent linear diffusion conditions which arise due to overlapping concentration profiles during the course of a cyclic voltammetric experiment [19,20,32,34,37,38,63]. Qualitative information regarding NP spacing has been reported by observing shifts in the peak potential, and changes in the magnitude of peak current and in the shape of the *i*–*E* wave with variations in active particle size and spacing as the potential is scanned slowly and linearly.

In this paper we report a theory and strategies for evaluating the intrinsic kinetic activity of NP ensembles and arrays under steady-state conditions due to convection. The theory draws on previous work related to modified electrodes [52–62,64–66] and ultramicroelectrode arrays and ensembles [67–77] where an electrode surface is largely inert except for the presence of micro- and nanoscopic active sites where redox reactions may take place and the current response is a function of the number and dimensions of the active sites and the fraction of blocking on the electrode surface. This situation is similar to that of a highly dispersed catalyst where NPs on a GCE support are separated by kinetically inactive areas. We demonstrate the importance of limiting current (i.e. mass transport condition) and fraction of inactive area when comparing SSVs recorded due to oxygen reduction at random, Pt NP clusters dispersed on a macro-glassy carbon inlaid disk electrode (GCE). We describe two approaches to calculating the intrinsic kinetic current density: a direct approach involving the electroactive surface area in which the mass transport and the inactive area effects are collectively separated from the kinetic controlled response in one step and a two-step approach involving the geometric surface area in which the mass transport contribution is separated first through an apparent intrinsic kinetic current density term from which the intrinsic kinetic current density is then extracted. The two approaches are shown to be equivalent within experimental error. Pt NPs were fabricated using reverse microemulsions (RME) [78–87] involving the stabilization of an aqueous core where the NPs are generated by a surfactant in a nonpolar solvent. Advantages of the RME method include the ability to control the NP size by adjusting the microemulsion water–surfactant molar ratio, the monodispersity of the NPs formed, and the generality of NP synthesis (e.g. metals and alloys [43,44,88–93], metal oxides [94–96], and organic polymers [97]).

2. Experimental

2.1. Materials

Sodium dioctylsulfosuccinate (Acros Organics, 96%), *n*-heptane (Acros Organics, 99%), dihydrogen hexachloroplatinate (IV),

($H_2PtCl_6{\cdot}6H_2O$, 99.9%, Alfa Aesar), sodium borohydride ($NaBH_4$, MP Biomedicals), sulfuric acid (H_2SO_4, Fisher, 95.5%), potassium permanganate ($KMnO_4$, Fisher), sodium hydroxide (NaOH, Fisher), anhydrous calcium sulfate ($CaSO_4$, Fisher), and deionized water (18 MΩ, Millipore Co., MA) were used as received.

2.2. Electrodes and instrumentation

Electrochemical measurements were carried out using a CHI 660B Electrochemical Workstation (CH Instruments, USA) and were conducted in a glass cell containing 0.1 M H_2SO_4. A saturated calomel reference electrode (SCE, CH Instruments, USA) separated from the main cell by a Vycor fritted glass sleeve and containing the same H_2SO_4 solution was used to prevent chloride contamination. A Pt wire (Goodfellow Metals, 1 mm diameter) served as a counter electrode. A glassy carbon electrode (GCE, 3 mm diameter GC disk surrounded by KEL-F, CH Instruments, USA) was polished with 0.05, 0.3, and 1 μm alumina and viewed under a Olympus BX 51 optical microscope (Olympus American Inc., NY).

A Buehler Ultramet III Sonic Cleaner was used in the reverse microemulsion Pt nanoparticle syntheses.

TEM and SEM images were taken at the University of Texas at Austin through the Texas Materials Institute and the Center for Nano- and Molecular Science and Technology respectively. TEM images were obtained on a JEOL 2010F transmission electron microscope which has a point image resolution of 0.194 nm. Carbon film-supported 300 mesh Cu TEM grids (C-Type B, Ted Pella, Inc.) were used. Each TEM grid was dipped vertically ten times in a NP RME/heptane solution prepared by dispersing 10 μL of NP RME in 5 mL of heptane in a glass vial, mixing gently, and letting the vial sit for 15 min. The TEM grid was then dried for 30–60 s under a high intensity lamp to evaporate the solvent. SEM images of representative NP/GCE samples were recorded on a LEO 1530 SEM instrument. NPs were deposited on a GCE that had been cut to 2 mm in height, thus preserving its circular dimensions. Due to the difficulty with charging of the NP/GCE samples due to the KEL-F insulator, the SEM images could only be acquired at 10.0 kV. TEM and SEM images were analyzed using NIH Image J software (http://rsb.info.nih.gov/ij/).

2.3. Reverse microemulsion (RME) synthesis of Pt NPs

Reverse microemulsions (RMEs) were made by mixing sodium dioctylsulfosuccinate (SDSS) surfactant in 10 mL of heptane, corresponding to a SDSS concentration of 0.1 M [98]. Pt NPs were prepared in the aqueous cores of the resulting reverse micelles by mixing a RME containing H_2PtCl_6 with a RME containing the reducing agent $NaBH_4$. The H_2PtCl_6 concentration in the Pt RME was optimized at 5.4×10^{-3} M in order to record a current above the GCE background. The concentration of $NaBH_4$ in the reducing RME was 8.7×10^{-3} M, representing an excess of $[NaBH_4]/[H_2PtCl_6] = 1.6$.

The Pt RME was prepared by dropwise addition of the aqueous H_2PtCl_6 solution into a 0.1 M SDSS/*n*-heptane mixture with vigorous stirring for 15 min followed by ultrasonication for an additional 15 min. The $NaBH_4$ RME was prepared by dropwise addition of the aqueous $NaBH_4$ solution into 0.1 M SDSS/*n*-heptane mixture with vigorous stirring for one minute followed by ultrasonication for one minute. The RMEs were then mixed and ultrasonicated for 1.5 h to form Pt NP RMEs.

The reverse micelle aqueous core influences the size of the Pt NPs and is determined by the molecular water-to-surfactant ratio, *W* [99,100],

$$W = \frac{[H_2O]}{[SDSS]} = \frac{V_{H_2O} d_{H_2O} / M_{H_2O} V_{hep}}{m_{SDSS} / M_{SDSS} V_{hep}} \quad (1)$$

where *V* represents volume; *d*, density; *M*, molar mass; and *m*, mass. In this work, values of $W = 2$, 10, and 30, corresponding to $V_{H_2O} = 36$, 180, and 540 μL, were used. These H_2O volumes were used in preparing the individual Pt and $NaBH_4$ RMEs in the corresponding *W* preparations.

The radius of the aqueous core of the reverse micelle is given by [99,100]

$$r\ (\mathrm{nm}) = 3\upsilon W / f_{SDSS}(W) \quad (2)$$

where υ refers to the molecular volume of water (3.0×10^{-29} m^3) and

$$f_{SDSS}(W)\ (\mathrm{nm}^2) = 0.596 - 0.468 \exp\{-0.401 (W)^{1/2}\} \quad (3)$$

where $f_{SDSS}(W)$ refers to the equilibrium area of the water/heptane interface covered by one SDSS molecule. Generally, Eqs. (2) and (3) are used to calculate a *W* value based on a desired NP radius and the resulting NP radius is determined by TEM. For $W = 2$, 10, and 30 RMEs (hereafter referred to as *W*2, *W*10, and *W*30 RMEs) prepared in this work, Eqs. (2) and (3) lead to calculated radii of 0.5, 1.9, and 4.9 nm. TEM images and histograms for Pt NPs from *W*2 and *W*30 RMEs are shown in Fig. 1. The particle sizes measured by TEM are larger than the aqueous core of the reverse micelles predicted by Eq. (2) and this discrepancy has been attributed to the dynamic nature of the reverse micelle preparation [81,91,101]. For example, the radius for the *W*2 NPs, as shown in the histogram, was 1.4 ± 0.1 nm. *W*30 NPs formed star-shaped clusters with radii of 7 ± 1 nm; within each cluster, the NPs have a radius of 2.4 ± 0.6 nm.

2.4. Pt NP dispersion on a glassy carbon electrode (GCE)

A GCE (3 mm diameter GC disk surrounded by insulator) was polished with 1, 0.3, and 0.05 μm alumina followed by ultrasonication for 5 min in deionized water.

NPs in the reverse micelles were deposited onto the GCE by gravity. First, the insulator surrounding the GC disk was covered with Teflon tape and the GCE was placed at the bottom of a reservoir (0.6 cm diameter, 8 cm length) that could hold approximately 2 mL of acetone. A known amount (μL) of NP RME was dispensed into the acetone and allowed to travel to the surface of the GCE over a timed period of 45 min. During this time, acetone destabilizes the reverse micelles thus releasing the NPs, which deposit onto the carbon and Teflon coated areas of the GCE. After 45 min., the acetone was slowly drained from the reservoir by creating a small gap between the GCE and the reservoir body. The NP-modified GCE (i.e. NP/GCE) was washed with acetone (by refilling and draining the reservoir) several times to remove residual surfactant and *n*-heptane followed by washing with deionized water in the same manner. The Teflon tape was removed, leaving only the NPs that adhered to the C disk area of the GCE. This procedure was repeated for *W*2, *W*10, and *W*30 compositions. The volume of the NP RME ranged from 10 to 200 μL in order to vary the NP coverage on the GCE surface. As the NP RME volume increases, the number of NPs on the C surface area increases with a resulting increase in the NP coverage.

2.5. Electrochemical experiments

After washing with deionized water, the deposited NPs were protected by a drop of deionized water and the NP/GCE assembly was transferred to an electrochemical cell containing 0.1 M H_2SO_4 which had been pre-purged with high purity Ar for 1 h followed by another half hour in the cell; an Ar blanket was maintained during all experiments. The electrode potential was cycled between −0.25 to 1.2 V vs. SCE at 0.1 V/s until a reproducible cyclic voltammogram (CV) was recorded. All potentials were converted

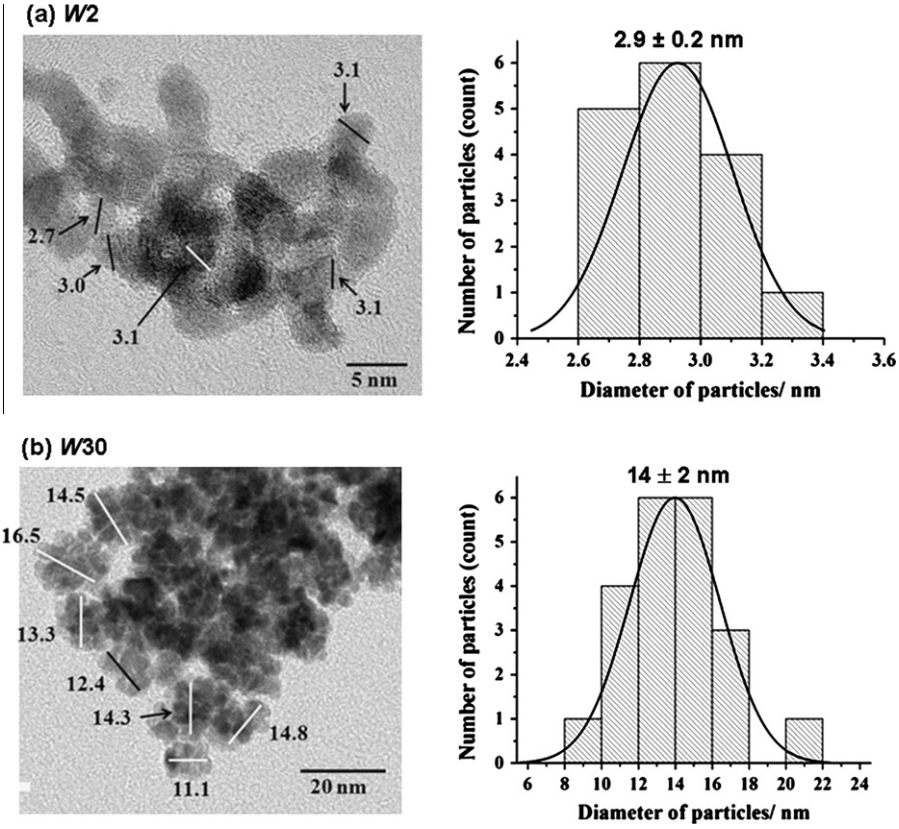

Fig. 1. HRTEM image of *W*2 (a) and TEM image of *W*30 (b) Pt NP RMEs. The errors are standard deviations.

off line and reported vs. SHE. These scans were used in determining the electroactive surface area of the NP/GCEs and for background subtraction in voltammograms recorded in saturated O_2 solution. The electrochemical active surface area, A_{ES}, was calculated from the charge over the hydrogen desorption region (Q_A) during the anodic scan of the CV recorded under continuous Ar purging and the charge required to form one monolayer of hydrogen per unit square centimeter of smooth Pt surface (i.e. 210 μC/cm^2 which corresponds to a hydrogen atom adsorbed for each Pt surface atom and a surface atomic density of 1.30×10^{15} atoms/cm^2) [102].

In O_2 reduction experiments, the solution was replaced with fresh 0.1 M H_2SO_4 that was pre-purged with research grade O_2 for 1 h, followed by another half hour in the electrochemical cell. Hydrocarbon impurities in the O_2 were removed by passing the gas through a series of traps containing 1 M $KMnO_4$, 1 M NaOH, anhydrous $CaSO_4$, and deionized water, consecutively. The glass capillary used to deliver O_2 into the solution was carefully placed at a constant distance from the surface of the NP/GCE and the gas pressure adjusted to give a bubble-by-bubble flow of O_2. The potential was scanned from 1.0 V to −0.1 V to 1.0 V vs. SCE (1.28 V to 0.18 V to 1.28 V vs. SHE) at 0.1 V/s.

2.6. SEM analyses of W2 and W30 Pt NP depositions

Fig. 2 shows SEM images of representative *W*2 and *W*30 Pt NP depositions for NP RME volumes of 20, 40, and 60 μL. The images indicate that NP agglomeration occurred resulting in clusters with radii larger than for single NPs in the TEM results. The range of NP cluster diameters is indicated for a specific image whereas Table 1 tabulates an average cluster diameter and the area fraction% over six SEM images. The average cluster size increases within the *W*2 group but remains approximately the same for the *W*30 group. The fraction of GCE surface covered by NP clusters increases within the *W*2 and *W*30 groups but these values are well below those predicted from the electrochemical active surface areas reported in a later section. The discrepancy is attributed to the limitation of SEM to image smaller NPs or NP clusters due to the charging of the sample, in addition to the various conversions of the images in the Image J analysis. Another reason for this discrepancy could be related to morphological changes of the electrode surface during cyclic voltammetry in acid. When cycling the NP ensemble potential up to 1.2 V vs. SCE, in addition to cleaning the electrode there is a redistribution of surface Pt atoms that dissolve and may redeposit onto different sites, generating a surface morphology that is different from the original.

3. Theory

3.1. The NP-modified surface

We approximate the behavior of ensembles of kinetically active NPs on a kinetically inactive surface by considering a circular inlaid disk electrode of radius R_D which is modified by spherical NPs of radius r_{NP} that are spaced a distance $2R_0$ center-to-center, as shown in Fig. 3a. The inactive zones are assumed to be circular and of radius R_0, with one NP in the center of each circular inactive zone. There are p circular zones distributed uniformly across the surface of the inlaid disk. The limit $R_0 = r_{NP}$ corresponds to NPs which are in physical contact with one another. This model is similar to those adopted in treatments of partially blocked electrode surfaces [52–62,64–66] and microelectrode arrays [67–77]. Both geometric surface area (or projected area), A_{GS}, of the supporting inlaid disk electrode and microscopic or electrochemical active surface area, A_{ES}, of the NPs play a role in the behavior of this modified electrode; their ratio may be written as

$$A_{ES}/A_{GS} = \gamma(1-\theta) \quad (4)$$

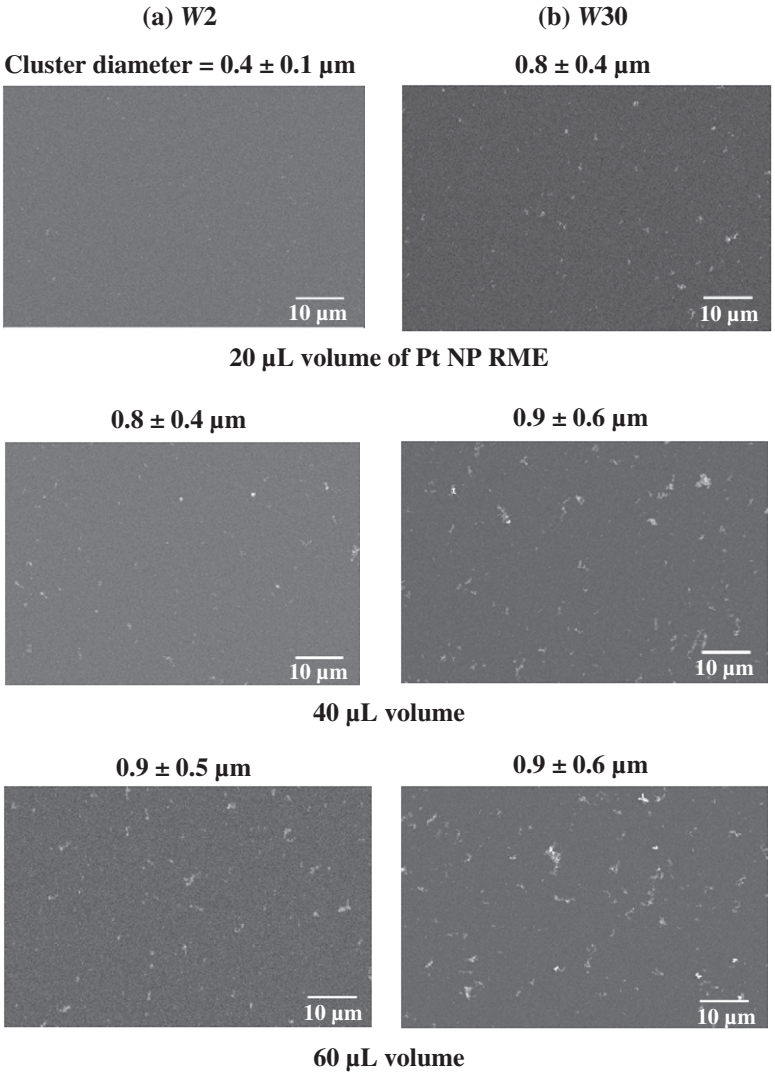

Fig. 2. SEM images of *W*2 (a) and *W*30 (b) depositions on a GCE with 20, 40 and 60 μL volumes of the respective Pt NP RMEs. The SEM images were acquired at 10.0 kV. The errors represent standard deviations.

Table 1
*W*2 and *W*30 deposition summary based on SEM images for volume aliquots, $V_{NP\ RME}$, of 20, 40 and 60 μL of NP RMEs. The data represents results from Image J analysis of the SEM images. Errors are standard deviations based on six images for each volume.

	Average cluster diameter (μm)	Area fraction (%)
Sample W2		
$V_{NP\ RME}$ = 20 μL	0.46 ± 0.08	0.1 ± 0.0
$V_{NP\ RME}$ = 40 μL	0.6 ± 0.3	0.4 ± 0.1
$V_{NP\ RME}$ = 60 μL	0.9 ± 0.2	0.6 ± 0.1
Sample W30		
$V_{NP\ RME}$ = 20 μL	0.80 ± 0.03	0.3 ± 0.0
$V_{NP\ RME}$ = 40 μL	0.8 ± 0.2	0.7 ± 0.2
$V_{NP\ RME}$ = 60 μL	0.9 ± 0.1	1.1 ± 0.2

The geometric area refers to the supporting circular inlaid GCE (i.e. $A_{GS} = \pi R_D^2 = p\pi R_0^2$, where R_D = 1.5 mm), whereas the electrochemical active surface area refers specifically to the spherical NPs (i.e. $A_{ES} = p4\pi r_{NP}^2$). When the kinetically inactive GCE surface is interrupted by active sites of nanometer dimensions, γ is related to the geometry of the active site. Thus, γ = 1, corresponds to active sites which are nanodisks of radius r_{ND} with $A_{ES} = p\pi r_{ND}^2$; γ = 2, to nanohemispheres of radius r_{NH} with $A_{ES} = p2\pi r_{NH}^2$; and γ = 4, to nanospheres of radius r_{NP}. The variable θ represents the fraction of the geometric surface that is inactive and $(1-\theta)$ corresponds to the fraction that is active. When the active sites are spherical NPs, A_{ES}/A_{GS} varies between 4 (i.e. θ = 0) and 0 (i.e. θ = 1). The fraction of inactive geometric surface area follows from Eq. (4) to:

$$\theta = 1 - \frac{A_{ES}}{4A_{GS}} = 1 - \left(\frac{r_{NP}}{R_0}\right)^2 \tag{5}$$

where A_{ES} and A_{GS} can be determined experimentally, and γ = 4 follows from the NP spherical geometry. The number of active NPs follows from A_{ES} and r_{NP} according to

$$p = \frac{A_{ES}}{4\pi r_{NP}^2} = \frac{(1-\theta)A_{GS}}{\pi r_{NP}^2} = \frac{A_{GS}}{\pi R_0^2} \tag{6}$$

Eq. (6) shows that for fixed values of $(1-\theta)$ and A_{GS}, the number of NPs decreases as the size of the NP increases, resulting in greater spacing between the NPs. In contrast, for fixed values of A_{GS} and r_{NP}, the number of NPs increases with $(1-\theta)$, and thus the distance between the NPs decreases. Table 2 tabulates the

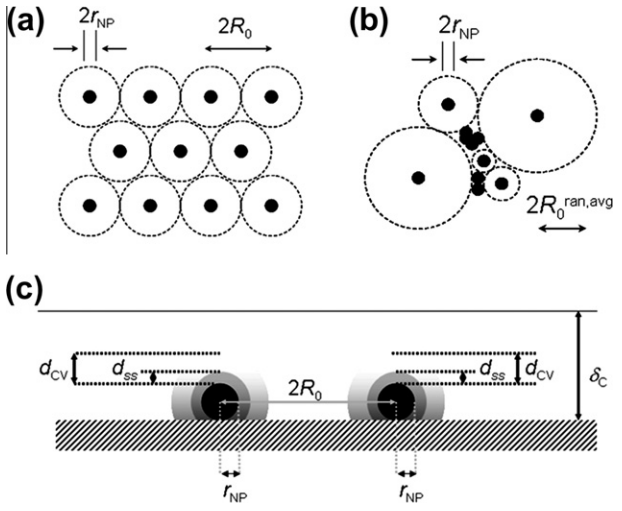

Fig. 3. Model for a surface with NP sites (shaded) of radius r_{NP}. (a) Top view of a uniform array with inactive circular zones (dotted circle) of radius R_0. (b) Top view of a random array with a distribution of inactive circular zones (dotted circle) of radius R_0^{ran} with an average radius $R_0^{ran,avg}$. (c) Schematic showing the different distances at spherical NPs distributed on a larger planar surface in the presence of convection.

number of regularly spaced spherical NPs calculated from Eq. (6) for a range of r_{NP}, R_0/r_{NP}, and $(1-\theta)$. This table indicates that there are a surprising number of NPs, even for small values of $(1-\theta)$.

The radius of each uniformly spaced, circular zone can be approximated by

$$R_0 \approx R_D/p^{1/2} \tag{7}$$

The NP density on the kinetically inactive support follows as

$$\rho_{NP} = \frac{p}{A_{GS}} = \frac{(1-\theta)}{\pi r_{NP}^2} = \frac{1}{\pi R_0^2} \tag{8}$$

and can be used to estimate the average NP spacing in a random array

$$R_0^{ran,avg} = \frac{0.25}{\sqrt{\rho_{NP}}} = 0.44R_0 \tag{9}$$

which follows from a distribution of random distances, R_0^{ran}, using the nearest-neighbor approximation [69,103]. Thus, a distribution of randomly-spaced NPs will, on average, be closer than those that are uniformly spaced, as shown in Fig. 3b.

3.2. Steady-state current at a NP-modified surface

For an irreversible reaction taking place at a kinetically inactive circular inlaid disk electrode modified with electrochemically active spherical NPs and in the presence of convection, the steady-state current can be represented by an inverse relationship involving a limiting current due to convection ($i_{L,C}$) [49] at an electrode that is completely covered with NPs (i.e. $\theta = 0$), a limiting current due to diffusion to the spherical nanoparticles ($i_{L,NP}$) [104–106] that are separated by a distance $2R_0$ and assuming that each NP acts individually, and a kinetic current (i_K) [49]. The resulting expression is similar to that used in describing the steady-state current at modified electrodes assuming a pin-hole model [49,59,60,62,107],

$$\frac{1}{i(E)} = \frac{1}{i_{L,C}} + \frac{1}{i_{L,NP}} + \frac{1}{i_K(E)} \tag{10}$$

where

$$i_{L,C} = nFA_{GS}^{\theta=0}C_O^* m_C \tag{11}$$

$$\begin{aligned} i_{L,NP} &= nFA_{ES}C_O^* m_{NP} = nFA_{ES}C_O^* \ell n(2) D_O/r_{NP} \\ &= nFA_{GS}^{\theta=0}C_O^*(2r_{NP}/R_0)^2 m_{NP} \end{aligned} \tag{12}$$

$$i_K(E) = nFA_{ES}C_O^* k_f(E) \tag{13}$$

and m is the mass transfer coefficient due to either convection to the geometric surface or to diffusion to NPs; all other variables have their usual electrochemical meaning. The geometric surface area for an electrode completely covered with spherical NPs is $A_{GS} = \pi R_D^2 + 4\pi R_D r_{NP} \approx \pi R_D^2$, where the face area of the supporting electrode described by the first term dominates over the area provided by the NP diameter described by the second term, as long as $R_D \gg r_{NP}$.

3.2.1. Theoretical limiting current

There are several distances and times that contribute to the manifestation of the mass-transfer controlled steady-state limiting current; these are shown in Fig. 3c. The magnitude of the solution diffusion layer due to convection is designated as δ_C and is defined as [49,107]

$$\delta_C = D_O/m_C \tag{14}$$

Additionally there is a steady-state diffusion length, d_{ss}, that must be established around an individual supported NP for it to display steady-state behavior; this distance follows from the spherical form of Fick's First Law and, assuming a linear concentration profile, is found to be [104–106,108]

$$d_{ss} = r_{NP}/\ell n(2) \tag{15}$$

where d_{ss} is measured from the surface of the spherical NP. The time required for d_{ss} to be established within a% of the steady-state is [108]

$$t_{ss} > \left(\frac{100r_{NP}}{a\ell n(2)}\right)^2 \left(\frac{1}{\pi D_O}\right) \tag{16}$$

Table 2
Matrix to estimate the number, p, of regularly spaced spherical NPs (Eq. (6)) under particular conditions of NP radius, r_{NP}, and spacing, R_0/r_{NP}, and fraction of electrode active area, $(1-\theta)$, on a GC surface of $A_{GS} = 0.0707$ cm^2. m_{NP} is the mass transfer coefficient for an individually supported spherical NP; it is defined as $m_{NP} = \ln(2)D_O/r_{NP}$.

r_{NP}(nm)	m_{NP}(cm/s)	R_0/r_{NP} $(1-\theta)$	500 4×10^{-6}	250 2×10^{-5}	100 1×10^{-4}	50 4×10^{-4}	10 0.01	5 0.04	2 0.25	1.5 0.44
0.5	250	p	4×10^7	2×10^8	9×10^8	4×10^9	9×10^{10}	4×10^{11}	2×10^{12}	4×10^{12}
1	125	p	9×10^6	4×10^7	2×10^8	9×10^8	2×10^{10}	9×10^{10}	6×10^{11}	1×10^{12}
5	25	p	4×10^5	1×10^6	9×10^6	4×10^7	9×10^8	4×10^9	2×10^{10}	4×10^{10}
10	12	p	9×10^4	4×10^5	2×10^6	9×10^6	2×10^8	9×10^8	6×10^9	1×10^{10}
50	2.5	p	4×10^3	1×10^4	9×10^4	4×10^5	9×10^6	4×10^7	2×10^8	4×10^8
100	1.2	p	900	4×10^3	2×10^4	9×10^4	2×10^6	9×10^6	6×10^7	1×10^8
250	0.50	p	144	576	4×10^3	1×10^4	4×10^5	1×10^6	9×10^6	2×10^7
500	0.25	p	36	144	900	4×10^3	9×10^4	4×10^5	2×10^6	4×10^6

A diffusion length due to the CV experiment, d_{CV} [109],

$$d_{CV} = \left(\frac{D_O RT}{nF\nu}\right)^{1/2} \quad (17)$$

which is also measured from the surface of the NP, will result as the potential is swept at a sweep rate ν over the time [109]

$$t_{CV} = RT/nF\nu \quad (18)$$

In our experiments $\nu = 0.100$ V/s, $n = 4$, and $D_O = D_{O2} = 1.8 \times 10^{-5}$ cm^2/s [28,110], leading to $d_{CV} = 11$ μm and $t_{CV} = 64$ ms. In addition to the lengths d_{ss} and d_{CV}, there is also the center–center distance, $2R_0$, between the NPs. A NP-modified surface will behave as a planar electrode at all times and in the presence or absence of convection when $r_{NP} = R_0$ (i.e. the NPs are immediately adjacent to each other) and when $R_0 < d_{ss}$ (i.e. the steady-state diffusion layers overlap). We also assume that $d_{CV} \ll R_D$ and $\delta_C \ll R_D$. The time to reach within 10% of a steady-state (Eq. (16)) is directly proportional to r_{NP}^2 and varies from 37 ns for a 1 nm radius spherical NP to 9 ms for a 500 nm radius spherical NP; these times are short in comparison to $t_{CV} = 64$ ms in our experiments.

In the absence of convection, the limiting current will be determined by the interplay of a time-dependent linear-diffusion term and a steady-state diffusion term due to the NPs. If the time scale of the experiment is sufficiently small, so that $d_{CV} \ll r_{NP}$, the NP-modified electrode will show a linear electrochemical response, except that the area will be $(1-\theta)$ times that of the fully covered electrode. This means that electrolysis of solution species occurs directly at each NP on the supporting electrode and there is no overlap of diffusion layers. This condition is generally difficult to reach when NPs are supported on a large, planar electrode. At longer times, $d_{ss} < d_{CV} < R_0$, so that each NP will show steady-state ultramicroelectrode (UME) behavior, and the steady-state current that results represents the sum of the steady-state current contributions from the individual NPs; this condition is also difficult to reach for NPs on a large, planar supporting electrode. When the time is such that the diffusion layers from the individual NPs grow together, overlap, and merge (i.e. $R_0 < d_{CV} < R_D$), the electrode behavior approaches that of the fully covered electrode with a total geometric area that includes both the NPs and the inactive area; a transient current results. For example, for arrays of regularly spaced NPs, with radii and spacings considered in Table 2 and under our experimental conditions, the total overlap mode would be expected for NPs of radii: $0.5 < r_{NP} < 10$ nm for all R_0/r_{NP} values in Table 2; $r_{NP} = 50$ nm, for $R_0/r_{NP} < 220$; $r_{NP} = 100$ nm, $R_0/r_{NP} < 110$; $r_{NP} = 250$ nm, for $R_0/r_{NP} < 44$; $r_{NP} = 500$ nm, for $R_0/r_{NP} < 22$. For randomly spaced arrays, a distribution of NP spacings are expected which, on average, are smaller than for a regularly-spaced distribution.

When convection also contributes to mass transport, a steady-state current results which is based on both convective and diffusive contributions, as Eq. (10) indicates. The relative importance of each of these contributions will be determined by the distance scales established by convection (i.e. δ_C) and diffusion (i.e. d_{ss}, d_{CV}), in addition to the NP spacing (i.e. $2R_0$) and size (i.e. r_{NP}), and the radius of the supporting electrode (i.e. R_D) as shown in Fig. 3(c). For $R_0 \ll d_{CV} \approx \delta_C \ll R_D$, the diffusion layers of individual NPs overlap and the geometric surface area of the supporting electrode appears to be uniformly active. Under these circumstances, convection probes the geometric surface and the steady-state current that results is driven by the rate of convection (i.e. $d_{CV} \approx \delta_C$ results in a steady-state current which increases as $d_{CV} > \delta_C$) with $i_L \propto m_C$. In contrast, for well-separated NPs where $d_{ss} \ll R_0 < \delta_C < d_{CV}$, NP coverage and diffusion is dominant so that $i_L \propto m_{NP}$ and reaches a constant independent of m_C. Between these limits, both convection and diffusion contribute to the steady-state limiting current i_L. The equation describing this behavior contains a steady-state limiting current due to convection to the active geometric surface area of a kinetically inactive-disk surface that is completely covered with kinetically active NPs and to diffusion to individual NPs that are spaced a distance of $2R_0$ center-to-center. The limiting current follows from Eqs. (10)–(12)

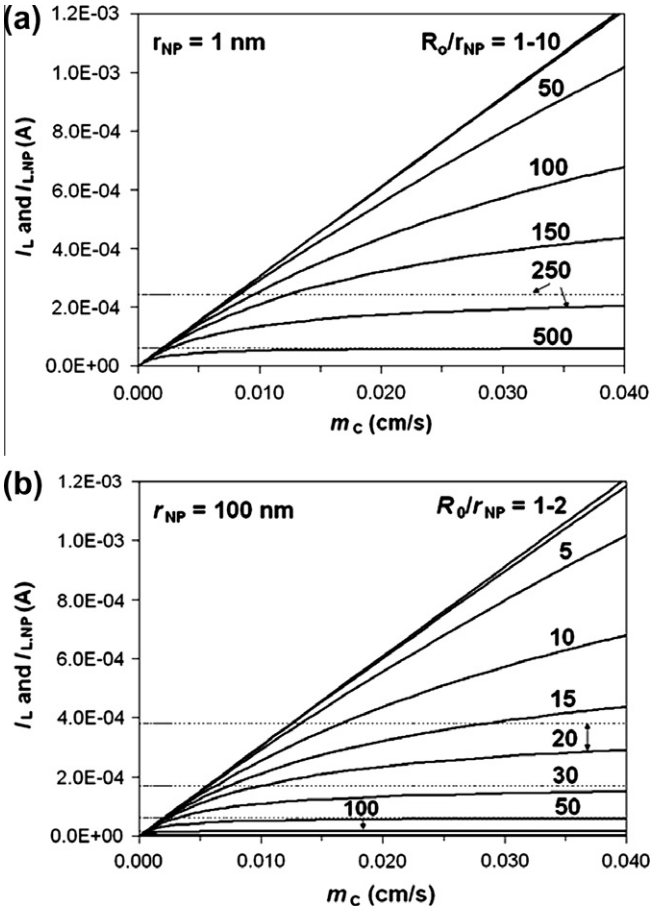

Fig. 4. The limiting current i_L (solid line) described by Eq. (19) as a function of m_C for NPs of 1 (a) and 100 nm (b) radii at R_0/r_{NP} spacings ranging from 1 to 500 on a kinetically inactive circular disk with a radius of 1.5 mm. The dotted lines correspond to $i_{L,NP}$ described by Eq. (12) for each r_{NP} and R_0/r_{NP}.

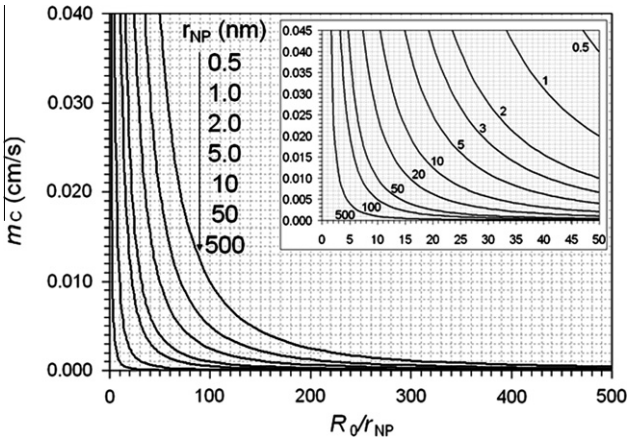

Fig. 5. Graph of the relationship between m_C and R_0/r_{NP} for the limiting current i_L (Eq. (19)) to be within 10% of i_{LC} Eq. (14). For a given r_{NP} and R_0/r_{NP}, m_C must be less than the value read from the graph (i.e. $m_C < 0.1 m_{NP}(2r_{NP}/R_0)^2$).

$$i_L = \frac{i_{L,C}}{1+\frac{i_{L,C}}{i_{L,NP}}} = \frac{nFA_{GS}^{\theta=0}C_O^* m_C}{1+\frac{m_C}{m_{NP}(2r_{NP}/R_0)^2}} = \frac{nFA_{GS}^{\theta=0}C_O^* m_C}{1+\frac{m_C}{m'_{NP}}} \quad (19)$$

From Eq. (12), the mass transfer coefficient for an individually supported spherical NP, $m_{NP} = \ln(2)D_O/r_{NP}$, increases as the NP radius decreases. Due to this inverse NP radius dependence, m_{NP} is generally much larger than the convective mass transport m_C (i.e. diffusion to a single NP is more efficient than convection). For example, spherical NPs of radii 1 and 100 nm have m_{NP} values of 125 and 1.25 cm/s respectively, as shown in Table 2. In comparison, a rotation rate of 2000 rad/s (e.g. an upper limit for a rotating disk) corresponds to $m_C \approx 0.040$ cm/s. Because the NPs are distributed across a large support surface, a collective diffusive mass transport coefficient, $m'_{NP} = (2r_{NP}/R_0)^2 m_{NP}$, can be defined which accounts for NP coverage on the supporting electrode surface. As R_0 increases relative to r_{NP}, the number of NPs on the surface decreases and thus m'_{NP} to the total surface decreases for a fixed r_{NP} and m_{NP}. As $R_0 \to \infty$, $i_L \to i_{L,NP}$ (Eq. (12)), and the limiting current is controlled by diffusion to the individual NPs on the surface. Similarly, for a fixed R_0/r_{NP} spacing, m'_{NP} will decrease with an increase in r_{NP} due to a corresponding decrease in m_{NP}. For spherical NPs of radii 1 and 100 nm, $m'_{NP} = 500$ and 5 cm/s respectively when $R_0 = r_{NP}$, while for $R_0 = 500r_{NP}$, $m'_{NP} = 0.002$ and 2×10^{-5} cm/s respectively. As shown by Eq. (19), the ratio of m_C to m'_{NP} controls the transition from $i_L = i_{L,C}$ to $i_L = i_{L,NP}$. In the limit of monolayer NP coverage (i.e. when $R_0 \approx r_{NP}$), $i_{L,NP} \gg i_{L,C}$ and $m'_{NP} \ll 1$, so that $i_L = i_{L,C}$; thus i_L depends on m_C but not NP coverage or radius. For $m_C < 0.1m_{NP}(2r_{NP}/R_0)^2$, i_L is within 10% of $i_{L,C}$. In the limit of large NP spacing, $i_{L,NP} \ll i_{L,C}$ and $(m_C/m'_{NP}) \gg 1$, so that $i_L = i_{L,NP}$; thus i_L is dependent on the NP radius and coverage but independent of m_C. When $m_c > 10m_{NP}(2r_{NP}/R_0)^2$, i_L is within 10% of $i_{L,NP}$. Between these two limits, both $i_{L,C}$ and $i_{L,NP}$ contribute to i_L; the magnitude of each contribution will depend on the number of NPs, their radius and spacing, and the mass transfer coefficients m_C and m_{NP}. A graph of i_L vs. m_C will show a linear variation of i_L with m_C (i.e. Eq. (11)) at small R_0 and approach a constant $i_{L,NP}$ (i.e. Eq. (12)) at larger R_0.

Fig. 4 shows i_L (solid line) as a function of m_C for NPs of $r_{NP} = 1$ (a) and 100 nm (b) at R_0/r_{NP} spacings ranging from 1 to 500 on a circular disk of $r_D = 1.5$ mm. There is marked departure of i_L from a linear dependence on m_C towards a constant value that approaches i_{NP} (dotted line) as R_0/r_{NP} increases; this departure from linearity occurs more quickly for $r_{NP} = 100$ nm. Figs. 5 and 6 show the relationship between m_C and R_0/r_{NP} over a range of r_{NP} when i_L is within 10% of $i_{L,C}$ or $i_{L,NP}$ respectively. These figures represent a summary of the information contained in Fig. 4 and generally

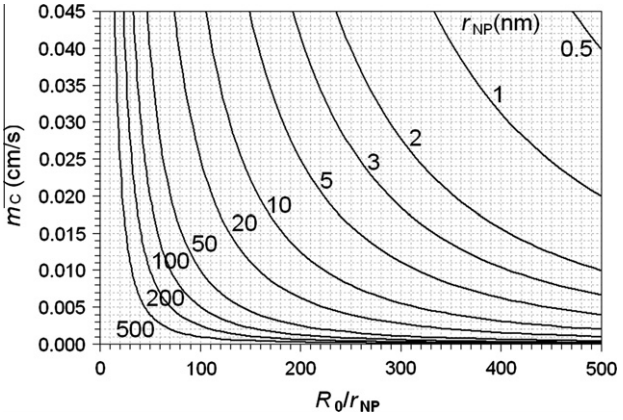

Fig. 6. Graph of the relationship between m_C and R_0/r_{NP} for the limiting current i_L (Eq. (19)) to be within 10% of i_{NP} Eq. (12). For a given r_{NP} and R_0/r_{NP}, m_C must be greater than the value read from the graph (i.e. $m_C > 10m_{NP}(2r_{NP}/R_0)^2$).

can be used to predict when i_L will be dominated by convection or by diffusion over a range of r_{NP} and R_0/r_{NP} values. For example, in Fig. 5, m_C values below the intersection of a m_C vs. R_0/r_{NP} point would be necessary to reach within 10% of the $i_L \approx i_{L,C}$ limit while those above that point would be necessary for the $i_L \to i_{L,NP}$ limit. In contrast, m_C values above the intersection of a m_C vs. R_0/r_{NP} point in Fig. 6 would be necessary to reach within 10% of the $i_L \approx i_{L,NP}$ limit while those below that point would be necessary for the $i_L \to i_{L,C}$ limit. For randomly spaced arrays of uniform size NPs, Eq. (9) indicates that NPs will, on average, be closer than those that are uniformly spaced. Thus, on Figs. 5 and 6, $i_{L,C}$ and $i_{L,NP}$ contributions to i_L of a single NP size distribution over a range encompassing both R_0/r_{NP} and a distribution of R_0^{ran}/r_{NP} distances would be considered. Similarly, for random distributions of both NP size and spacing, $i_{L,C}$ and $i_{L,NP}$ contributions to i_L covering a range encompassing R_0/r_{NP} and a distribution of R_0^{ran}/r_{NP} distances over a range of NP sizes would be considered.

3.2.2. Experimental limiting currents

We now briefly consider experimental parameters from our experiments in order to show that both i_{NP} and $i_{L,C}$ are necessary in the limiting current expression of Eq. (19). In our O_2 reduction experiments, $C_O^* = [O_2, \text{sat}] = 1.12 \times 10^{-6}$ mol/cm^3, $D_O = D_{O2} = 1.8 \times 10^{-5}$ cm^2/s [28,110], and $A_{GS} = 0.0707$ cm^2. The electroactive area A_{ES} ranges from 2.9×10^{-3} cm^2 to 0.13 cm^2 corresponding to a fraction of inactive area, θ, ranging from 0.99 to 0.53, respectively, according to Eqs. (4) and (5). For $\theta = 0.53$, Eqs. (4), (5), and (9), in addition to Table 2, predict a ratio $R_0/r_{NP} = 1.5$ for a uniform distribution and a random distribution of $R_0^{ran}/r_{NP} < 3$ with $R_0^{ran,avg}/r_{NP} \approx 0.53$ over the range of NP sizes considered in Table 2. These values correspond to high NP coverage. For $\theta = 0.99$, representing comparatively lower NP coverage, $R_0/r_{NP} = 10$ (uniform distribution) and a random distribution of $R_0^{ran}/r_{NP} < 16$ with $R_0^{ran,avg}/r_{NP} \approx 3.6$ are predicted.

SEM images (Fig. 2) show that the GCE surface consists of randomly distributed NP clusters (and probably smaller single NPs that are undetected by the SEM) rather than uniformly distributed single NPs. The cluster radii from the SEM images range from (230 ± 40) nm to (400 ± 100) nm for *W*2 and (400 ± 15) nm to (450 ± 50) nm for *W*30 while single NP radii based on TEM images (Fig. 1) were found to be (1.4 ± 0.1) nm for *W*2 and (2.5 ± 0.5) nm to (7.0 ± 1) nm for *W*30. Thus, in terms of NP size distribution, we considered a broad range of radii from 1 to 500 nm on any one supporting electrode surface for any *W* preparation. For $\theta = 0.53$, one predicts that a $i_L = i_{L,C}$ limit will be reached for $m_C \ll 0.045$ cm/s (Fig. 5) and the $i_L = i_{L,NP}$ limit for $m_C \gg 0.045$ (Fig. 6). From the limiting current of a $\theta = 0.53$ polarization curve ($i_L = 63$ μA, Fig. 10), a mass transfer coefficient of 0.002 cm/s was calculated according to Eq. (11), which is well below the limit necessary for $i_L = i_{L,C}$ for all spacings and NP size. For $\theta = 0.99$, an $i_L = i_{L,C}$ limit will be reached for $m_C \ll 0.001$ ($r_{NP} = 500$ nm), 0.005 ($r_{NP} = 100$ nm), 0.010 ($r_{NP} = 50$ nm), 0.040 ($r_{NP} = 1$–10 nm) cm/s for $R_0/r_{NP} = 10$ (uniform spacing, Fig. 5), and $m_C \ll 0.001$ ($r_{NP} = 500$ nm), 0.002 ($r_{NP} = 100$ nm), 0.003 ($r_{NP} = 50$ nm), 0.010 ($r_{NP} = 20$ nm), 0.020 ($r_{NP} = 10$ nm), 0.041 ($r_{NP} = 5$ nm), 0.045 ($r_{NP} = 3$–0.5 nm) cm/s, for a distribution of $R_0^{ran}/r_{NP} \leqslant 16$ (random spacing, Fig. 5) with $R_0^{ran,avg}/r_{NP} \approx 3.6$. An $i_L = i_{L,NP}$ limit will be reached for $m_C \gg 0.045$ cm/s (Fig. 6) for both uniform and random spacing. From the limiting current of a $\theta = 0.99$ polarization curve ($i_L = 20$ μA, Fig. 10), a mass transfer coefficient of 0.001 cm/s was calculated according to Eq. (11), which is not sufficiently slow for $i_L = i_{L,C}$ or sufficiently fast for $i_L = i_{L,NP}$ behavior for the larger NPs (i.e. 200–500 nm range); thus the limiting current in this case is likely a combination of slow convection and diffusion, which in part contributes to the variation in the limiting current values that we observed at large values of θ.

3.2.3. General steady-state current expressions

Based on the considerations in the previous section, the $(1/i_{L,NP})$ term cannot be ignored under conditions of large NP size, large θ, and slow convection so that Eq. (10) is written as

$$\frac{1}{i(E)} = \frac{1}{i_L} + \frac{1}{i_K(E)} \tag{20}$$

where i_L is given by Eq. (19). At constant m_C and m'_{NP}, i_L is constant and Eq. (20) can be rewritten as

$$\frac{1}{I(E)} = \frac{i_L}{i(E)} = 1 + \frac{i_L}{i_K(E)} = 1 + \frac{i_L}{j_K(E)A_{ES}} = 1 + \frac{j_L}{j_K(E)} = 1 + \frac{i_L/\gamma(1-\theta)A_{GS}}{j_K(E)} \tag{21}$$

where $\gamma = 4$ for spherical NPs and $I(E)$ is dimensionless normalized current based on the $i(E)/i_L$ ratio. The kinetic current density, $j_K(E) = i_K(E)/A_{ES}$, is due entirely to the intrinsic kinetics of the electron transfer. The limiting current density, $j_L = i_L/A_{ES} = i_L/4(1-\theta)A_{GS}$, includes effects of both convective and diffusion mass transport and the fraction of inactive geometric electrode area (or the fraction of active geometric electrode area) on the behavior of the NP electrode assembly operating under mixed mass transport and kinetic control. Thus, Eq. (21) indicates that the mass transport and inactive area effects can be collectively separated from the kinetic controlled response. This separation is performed by extracting the intrinsic kinetic current density, $j_K(E)$, from the slope of the linear dependency between $1/I$ and j_L at each potential, according to Eq. (21). We refer to this as the direct approach for the calculation of $j_K(E)$.

Eqs. (20) and (21) can also be written entirely in terms of current densities by multiplying by A_{ES}

$$\frac{1}{j(E)} = \frac{1}{i/A_{ES}} = \frac{1}{j_L} + \frac{1}{j_K(E)} \tag{22}$$

so that $j_K(E)$ can be determined from the intercept of the linear dependency between $1/j$ and $1/j_L$. This is another method of directly calculating $j_K(E)$ and is equivalent to the direct approach procedure described based on Eq. (21); it is also similar to conventional Koutecky–Levich plots [49],

One can also calculate $j_K(E)$ using a two-step approach based on equation (20) where current is divided by A_{GS} and, with use of Eq. (4),

$$\frac{A_{GS}}{i(E)} = \frac{A_{GS}}{i_L} + \frac{A_{GS}}{i_K(E)} = \frac{A_{GS}}{i_L} + \frac{1}{j_K(E)\gamma(1-\theta)} = \frac{A_{GS}}{i_L} + \frac{1}{j_K^{app}(E)} \tag{23}$$

an apparent kinetic current density, $j_K^{app}(E)$, can then be calculated as a function of potential which is related to the intrinsic kinetic density, $j_K(E)$, through the relationship

$$j_K^{app}(E) = \gamma(1-\theta)j_K(E) = 4(1-\theta)j_K(E) \tag{24}$$

where $\gamma = 4$ for spherical NPs. This apparent kinetic current density has contributions relating to the kinetic activity of the material ($j_K(E)$) and to the fraction of inactive geometric area (θ). Based on Eq. (24), the intrinsic or real kinetic current density (i.e. $j_K(E)$ corresponding to $\theta = 0$) at each potential can be calculated by extrapolating the linear dependence $j_K^{app}(E)$ vs. θ to $\theta = 0$. This represents a hypothetical situation where the entire geometric area of the disk electrode is covered by NPs, but which cannot be reached practically since it is not possible to completely cover the surface of a disk with a monolayer of spherical particles. The factor of 4 arises due to the fact that the particles are spherical while the fraction of inactive area is related to the projected area of these spheres onto the total flat geometric area.

4. Results and discussion

4.1. Electrochemical active surface area determination

Fig. 7 shows the cyclic voltammograms (CV) recorded for NP/GCEs immersed in deaerated 0.1 M H_2SO_4. The potential was cycled between 0.03 V to 1.48 V vs. SHE at 100 mV/s until a steady CV was obtained. The CVs were recorded for NP/GCEs where the NPs were synthesized with *W*2 RMEs, and dispersed on a GCE in 20, 40, and 60 μL volumes as described in the experimental section. Each CV displays the hydrogen region at potentials more negative than 0.35 V vs. SHE, the formation of the oxide at potentials more positive than 0.8 V, the reduction of the oxide at potentials between 1.2 V and 0.5 V, and the double layer region between 0.5 to 0.35 V. The current represents the difference between the current of the NP/GCE and that of the bare GCE, also shown in Fig. 7. This current increases as the NP RME aliquot increases from 20 to 60 μL. Similar CVs were recorded for NP/GCEs prepared with *W*10 and *W*30 NP RMEs with dispersion aliquots ranging from 10 to 190 μL. The stability of the NP/GCE surface was monitored over 24 h with little change in the recorded CVs.

The electrochemical active surface area (A_{ES}) of the NP/GCEs was determined from the charge in the hydrogen desorption region of the CV. This charge was calculated by subtracting the current due to the double-layer charging, integrating the anodic current of the hydrogen region and dividing by sweep rate. The A_{ES} (in cm^2) was then calculated using the constant 210 μC/cm^2 which assumes monolayer coverage of Pt NPs with atomic H [102].

The relationship between A_{ES}, *W*, and NP RME dispersion volume was found to be linear for the *W* and dispersion volumes con-

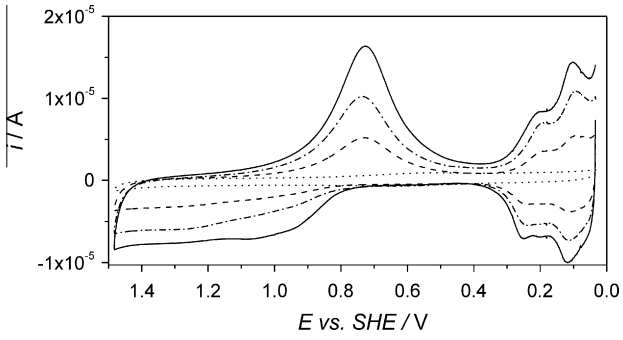

Fig. 7. Cyclic voltammograms (CVs) for Pt NP/GCEs in 0.1 M H_2SO_4 deaerated with Ar. Aliquots of a *W*2 NP RME corresponding to 20 (dash line), 40 (dot dash line) and 60 μL (solid line) were dispersed on a GCE as described. The electrode potential was cycled at 100 mV/s between 0.03 V and 1.48 V vs. SHE until a constant CV was obtained. Background subtracted CVs were obtained after subtraction of the CV measured on a bare GCE under the same conditions (dotted line).

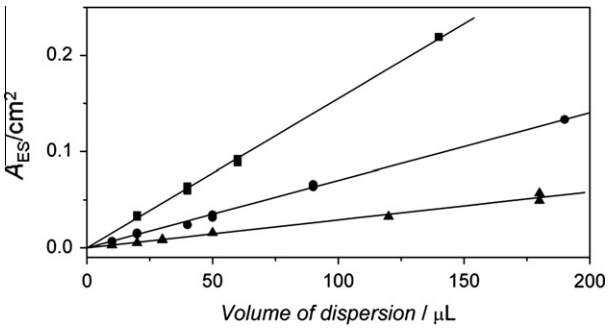

Fig. 8. Electroactive surface area (A_{ES}) as a function of the dispersion volume of *W* = 2 (■), 10 (●) and 30 (▲) Pt NP RMEs. Solid lines are the correlations using a linear function with a zero intercept.

sidered in this work, as Fig. 8 shows. Good agreement was found between repeated experiments with the same and new NP RME preparations. A_{ES} increases with increasing dispersion volume for a specific *W* indicating that more NPs are deposited on the GCE surface. Fig. 8 shows a decrease in A_{ES} from *W*2 to *W*30, for the same volume of dispersion, which may arise due to the increase in size of the entire reverse micelle from $W = 2$ to $W = 30$. For the same volume of dispersion, there will be fewer reverse micelles in a 20 μL volume of *W*30 microemulsion than for the *W*2 microemulsion. The *W*2 NPs also have a radius that is smaller than that of the *W*30 NPs. Thus the overall surface area of a *W*2 NP or cluster is more accessible than that of a larger *W*30 NP or cluster leading to a larger A_{ES}

4.2. Oxygen reduction studies

Fig. 9 shows current–potential curves (i.e. polarization curves) for O_2 reduction in O_2-saturated 0.1 M H_2SO_4. These curves were recorded using potential scans performed from positive to negative potentials (i.e. negative scans) and from negative to positive potentials (i.e. positive scans). A slow, stream of O_2 was maintained in close proximity to the electrode as described previously.

As shown in Fig. 9, a steady-state response for O_2 reduction was reached on the NP/GCE electrode under convection in contrast to its transient response due to planar diffusion in the absence of convection. The CV for O_2 reduction at a uniform Pt electrode is also shown and the similarity to that recorded at the NP/GCE is attributed to the moderately high coverage of Pt NPs on the GC surface (i.e. $(1-\theta) = 0.18$ corresponding to $R_0/r_{NP} = 2.4$ and $R_0^{ran,avg}/r_{NP} \approx 1.1$). Differences observed between the positive and the negative scans of the steady-state CV are attributed to the different initial states of the surface of the GCE-supported NPs for each scan. In the negative scan, the NPs start with an oxidized surface that is poorly active for O_2 reduction and the reduction of platinum oxide is required to observe significant O_2 reduction currents. This causes the onset potential to shift to more negative potentials when compared to that of an oxide-free NP surface as measured on a positive scan [111]. Thus, only positive scans were analyzed in this work.

Fig. 10 shows background-subtracted O_2 reduction curves that were normalized with respect to their limiting current values for NP/GCEs prepared from: (a) *W*2; (b) *W*10; and (c) *W*30 RMEs. A background current–potential curve measured on each electrode in deaerated solution was subtracted from the measured polarization curves in oxygenated solution to obtain the dependence of the O_2 reduction current on electrode potential. As potential decreases from 1.0 V to 0.2 V vs. SHE, there is a transition of the current from kinetic control at foot of the voltammogram, to mixed kinetic/transport control in the escarpment region of the voltammogram, and finally to mass transport control on the limiting current plateau. The potential range where the electrode operates under kinetic and mixed kinetic/transport control is a function of the mass transport conditions (e.g. i_L, Eq. (19)), of the fraction of inactive GC area (θ, Eq. (5)), and of the kinetics of the electron transfer ($i_K(E)$, Eq. (13)). The determination of i_L for those voltammograms with larger fractions of inactive areas (i.e. $\theta \geqslant 0.98$) was difficult because proton reduction began before the current reached a true mass transport limiting value. The mass transport and θ dependencies are established by Eqs. (21)–(24). Inspection of Fig. 10 generally shows that more negative potentials are needed to reach the limiting current region and that the *i*–*E* slope decreases in the mixed control region within each *W* group as θ increases. For those normalized voltammograms having unequal i_L currents, the kinetic rate relative to the mass-transport rate changes and plays a role in the decreasing steepness of the voltammogram, as shown by the open symbols in Fig. 10. These kinetic effects are similar to those seen in ultramicroelectrode (UME) studies where the mass-transport rate is increased by decreasing the size of the UME [108,112–114] or in scanning electrochemical microscopy (SECM) studies where the mass-transport rate is increased by decreasing the distance between a tip UME and underlying substrate electrode [115–117].

A group of three O_2 reduction curves measured under the same mass transport conditions (i.e. the same limiting current) and the same kinetic behavior (i.e. the same NP type, *W*10), is highlighted in Fig. 10 (solid symbols). With fixed kinetic behavior, these plots show the effect of changing only the fraction of inactive GCE area, with θ increasing as 0.53, 0.77, and 0.89. Since the kinetic behavior is fixed for this set of voltammograms, the slope in the escarpment region of the voltammogram does not change, as comparison of the solid symbols in Fig. 10b demonstrates.

Fig. 11 shows a direct comparison of polarization curves obtained using the same mass transport conditions on electrodes with similar fractions of inactive area (i.e. similar A_{ES}) but different *W* values. Comparisons made at $\theta = 0.77$ and $\theta = 0.88$ for *W*2 and *W*10 NPs, and at $\theta = 0.94$ for *W*10 and *W*30 NPs demonstrate a

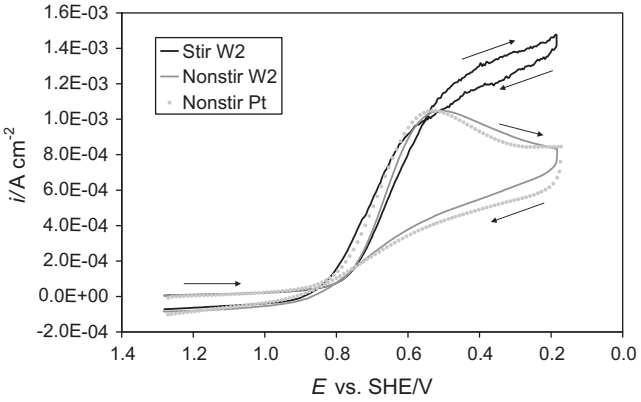

Fig. 9. CVs (at $v = 0.100$ V/s) for a Pt NP/GCE ($\theta = 0.82$, corresponding to $R_0/r_{NP} = 2.4$, $R_0^{ran,avg}/r_{NP} = 1.1$) in stirred (solid black line) and unstirred (solid grey line) 0.1 M H_2SO_4 saturated with O_2 at 1 atm. The arrows indicate the direction of the potential scans. The CV for a uniform Pt electrode (1.0 mm radius, light grey solid dots) in unstirred 0.1 M H_2SO_4 saturated with O_2 at a pressure of 1 atm is also shown.

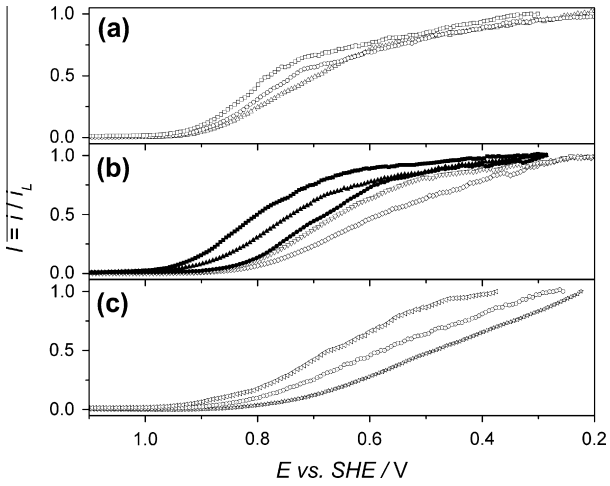

Fig. 10. Normalized oxygen reduction polarization curves of Pt NP/GCEs from NP RMEs *W*2 (a), *W*10 (b) and *W*30 (c) in 0.1 M H_2SO_4 saturated with O_2 at 1 atm. The values of the limiting current (i_L) and of the fraction of inactive area (θ) for each polarization curve are: (a) $i_L = 92$ μA, $\theta = 0.69$ (□); $i_L = 72$ μA, $\theta = 0.79$ (○); $i_L = 52$ μA, $\theta = 0.83$ (Δ); (b) $i_L = 63$ μA, $\theta = 0.53$ (■); $i_L = 62$ μA, $\theta = 0.77$ (▲); $i_L = 62$ μA, $\theta = 0.89$ (●); $i_L = 57$ μA, $\theta = 0.95$ (▽); $i_L = 32$ μA, $\theta = 0.98$ (◇); (c). $i_L = 59$ μA, $\theta = 0.82$ (◁); $i_L = 47$ μA, $\theta = 0.94$ (☉); $i_L = 20$ μA, $\theta = 0.99$ (☆).

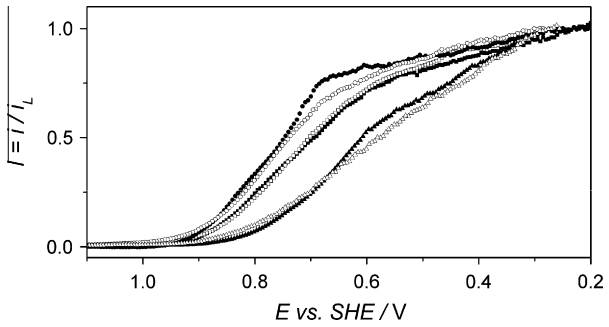

Fig. 11. Normalized O_2 reduction polarization curves of selected Pt NP/GCEs in 0.1 M H_2SO_4 saturated with O_2 at 1 atm. The values of the limiting current (i_L), the fraction of inactive area (θ) and the NP RME *W* for each polarization curve are: i_L = 62 μA, θ = 0.77, *W*10 (○); i_L = 62 μA, θ = 0.77, *W*2 (●); i_L = 52 μA, θ = 0.88, *W*10 (□); i_L = 52 μA, θ = 0.88, *W*2 (■); i_L = 50 μA, θ = 0.94, *W*30 (Δ); i_L = 50 μA, θ = 0.94, *W*10 (▲).

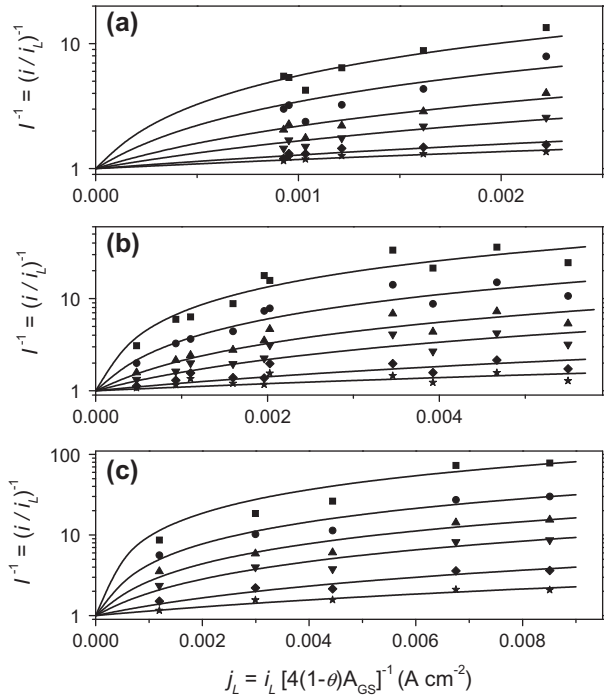

Fig. 12. Inverse normalized O_2 reduction current as a function of j_L for Pt NP/GCEs from *W*2 (a), *W*10 (b) and *W*30 (c) NP RMEs, obtained from polarization curves (Fig. 10) at electrode potentials of 0.5 (★), 0.6 (♦), 0.7 (▼), 0.75 (▲), 0.8 (●) and 0.85 V (■).

similarity in the polarization curves. To make quantitative comparisons, it is necessary to calculate the kinetic current density free of mass transport and θ effects at each potential from the experimental curves. To carry out this operation, two different approaches were used as described by Eqs. (20)–(24). These approaches differ from each other only in the steps that are followed to separate the contributions of mass transport and inactive area phenomenon from the experimental global response.

4.2.1. Direct approach for calculation of $j_K(E)$

In this approach, the mass transport and the inactive area effects are collectively separated from the kinetic controlled response in one step. This was performed by extracting the kinetic current density from the slope of the linear dependency between I^{-1} and j_L at each potential, according to Eq. (21).

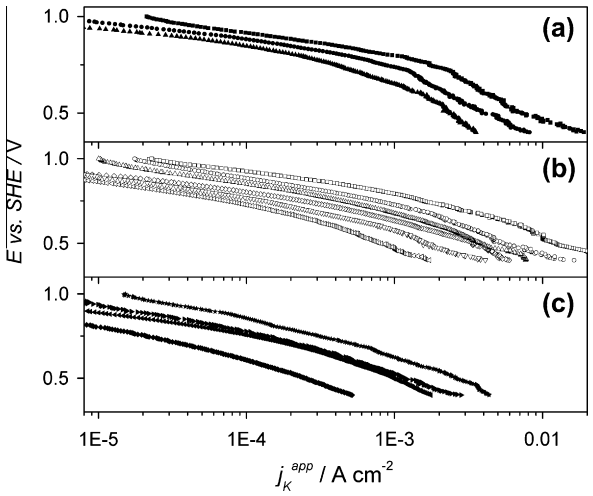

Fig. 13. Tafel plots of apparent kinetic current density (j_K^{app}) for O_2 reduction as a function of electrode potential for Pt NP/GCEs from *W* 2 (a), *W*10 (b), *W*30 (c) NP RMEs, and inactive area fractions (θ) of (a) 0.69 (■), 0.77 (●), 0.88 (▲); (b) 0.53 (□), 0.77 (○), 0.88 (Δ), 0.95 (◇), 0.94(▽), 0.98 (◁); (c) 0.83 (★), 0.94 (♦), 0.96 (◄), 0.99 (♦), in 0.1 M H_2SO_4 saturated with O_2 at 1 atm.

Plots of experimental I^{-1} obtained from the polarization curves vs. the respective experimental j_L values are shown in Fig. 12 for NP/GCEs from *W*2, *W*10, and *W*30 NPs at selected potentials. These plots are presented on a logarithmic scale to better illustrate the trends at more negative potentials where the normalized currents are close to unity. The correlations of these dependencies with Eq. (21) were acceptable and the values of $j_K(E)$ were calculated from the fitted slopes. Fig. 15a shows the resulting *E* vs. j_K curves, or Tafel plots, which allow the comparison and analysis of the pure kinetic response or intrinsic activity of the active NP/GCEs from *W*2, *W*10, and *W*30 NP RMEs.

4.2.2. Two-step approach for calculation of $j_K(E)$

In this approach, the contribution of mass transport is separated first on each individual curve according to Eq. (23) leading to the calculation of an apparent kinetic current density, j_K^{app}. This apparent kinetic current density arises through the use of A_{GS} rather than A_{ES} in treating current data and thus has contributions from both

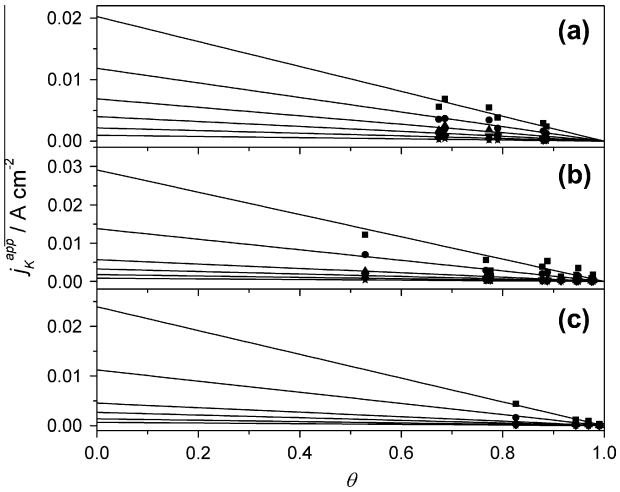

Fig. 14. Apparent kinetic current density (j_K^{app}) for O_2 reduction as a function of the fraction of inactive area (θ) for Pt NP/GCEs from *W*2 (a), *W*10 (b), and *W*30 (c) NP RMEs, obtained from Tafel plots (Fig. 13) at selected electrode potentials of 0.5 (★), 0.6 (♦), 0.7 (▼), 0.75 (▲), 0.8 (●) and 0.85 V (■) vs. SHE. Solid lines are correlations using the linear relationship $(j_K^{app}) = 4j_K(1-\theta)$.

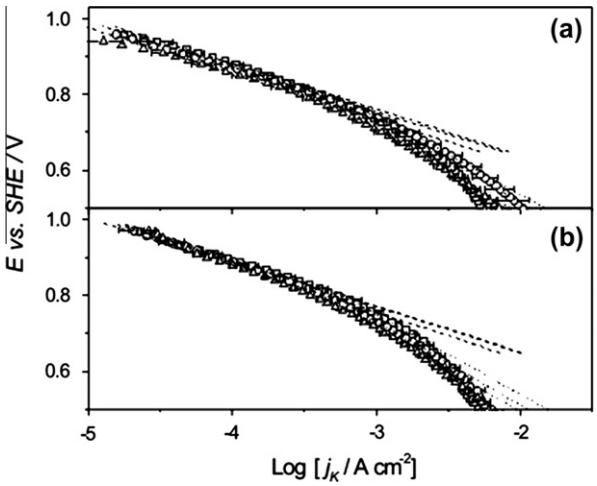

Fig. 15. Tafel plots of the logarithmic kinetic current density (j_K) for O_2 reduction as a function of electrode potential for Pt NP/GCEs from *W*2 (□), *W*10 (○) and *W*30 (Δ) NP RMEs, obtained following the direct (a) and two-step (b) approaches. In all cases, linear correlations in the potential ranges 0.9 V > *E* vs. SHE > 0.75 V (dash lines) and 0.75 V > *E* vs. SHE > 0.6 V (dot lines) resulted in Tafel slopes of 121 ± 2 mV/dec and 219 ± 6 mV/dec, respectively.

Table 3
Exchange current density, j_o, calculated from the Tafel plots (Fig. 15) in the 121 mV/dec slope region. NP/GCEs were prepared from *W*2, *W*10, and *W*30 RMEs and steady-state CVs were recorded in 0.1 M H_2SO_4 saturated with O_2 at 1 atm. Errors are standard deviations from the correlations.

W	j_o (A cm^{-2}) × 10^7	
	From direct approach	From two-step approach
2	1.3 ± 0.4	1.9 ± 0.3
10	1.0 ± 0.4	1.5 ± 0.4
30	0.8 ± 0.5	1.4 ± 0.4

the intrinsic activity of the material and the fraction of inactive area according to Eq. (24). Some of the resulting curves calculated in the potential range 1.0 V > *E* vs. SHE (V) > 0.4 are shown in Fig. 13 where the Tafel curves are displaced negatively with increasing θ.

The real kinetic current density (i.e. $j_K(E)$) in the absence of inactive area at each potential was calculated according to Eq. (24) by extrapolation of the linear $j_K^{app}(E)$ vs. θ dependence to $\theta = 0$, a limit that represents a hypothetical situation where the entire geometric area of the disk electrode is covered by Pt NPs. As explained in the theory section, this limit cannot be reached in practice because it is not possible to completely cover the surface of a disk with a monolayer of spherical NPs. Plots of experimental $j_K^{app}(E)$ obtained from the polarization curves vs. the corresponding θ values are shown in Fig. 14 at selected potentials. These plots include respective linear correlations carried out using Eq. (24), which represent the trend of the experimental values. That is, there is a clear increase in $j_K^{app}(E)$ as *E* becomes more positive and as θ decreases. The values of $j_K(E)$ at each potential were calculated from these correlations and graphed in the Tafel plots of Fig. 15b.

4.2.3. Comparison and implication of $j_K(E)$ results from the direct and two-step methods

The direct and two-step approaches are equivalent and resulting $j_K(E)$ vs. *E* dependencies should be similar. However, because both methods involve regression procedures using different functions, it is likely that each experimental value will have different weights in each procedure so that the results of the correlations will not be identical. This can be observed in Fig. 15, which shows the Tafel plots *E* vs. $j_K(E)$ obtained using the direct approach (a) and the two-step approach (b) on *i* vs. *E* data recorded on the NP/GCE electrodes. While showing slight differences due to statistical uncertainties, both sets of Tafel plots show very similar characteristics. The dependencies obtained for each NP/GCE do not show clear differences between them since all of the three $j_K(E)$ values at each potential lie within the same uncertainty boundaries. They all present a well-defined linear region with a Tafel slope of 121 ± 2 mV/dec at more positive potentials (0.9 V > *E* vs. SHE > 0.75 V) and another linear region with slope of 219 ± 6 mV/dec in the potential range 0.75 V > *E* vs. SHE > 0.6 V. Similar behavior was observed for O_2 reduction on C-supported single particle Pt electrodes [28]. The exchange current density (j_o) values calculated from extrapolation of the linear region of 121 mV/dec to *E* = 1.23 V vs. SHE are tabulated in Table 3. The *E* vs. $j_K(E)$ curves are representative of the intrinsic electrocatalytic activity of each electrode for the ORR, free of mass transport and inactive area effects. Any effect on the kinetics of this reaction should be manifested as a clear change in these plots. The absence of a clear change in these plots indicates that the intrinsic electrocatalytic activity of the NP/GCEs considered was similar. We attribute this to the slow convection used in probing electrocatalytic activity in addition to the presence of a distribution of nm-sized NP clusters that are larger than the 1–2 nm range where NP size effects have been reported [35].

5. Conclusions

The behavior of NP ensembles on a kinetically inactive electrode support can be best understood if the effects due to mass transport, kinetics (i.e. the intrinsic activity of the NPs), and the fraction of inactive area on the geometric support due to NP spacing can be separated. This separation is most easily achieved under steady-state conditions where the *i* vs. *E* response is limited by the kinetics of the reaction under investigation rather than by the mass transport of the reacting species. When the geometric support is large, steady-state conditions are most easily reached using convection. The simplest NP electrode system involves bare NPs attached to an inactive electrode support in the absence of binders such as Nafion. In this work, NPs were synthesized using the RME method and the resulting NPs were distributed on a GCE surface. Though TEM images showed synthesis of NPs in the nanometer range, SEM images indicated that agglomeration of the NPs occurred as they were randomly distributed on the GCE surface resulting in NP clusters of sub-micrometer dimensions which were too large to observe the kinetic effects that have been reported on NP distributions in the 1–2 nm range.

Two complimentary methods (i.e. a direct and two-step approach) of processing steady-state current data were used to calculate the intrinsic kinetic activity (i.e. as $j_K(E)$, the kinetic current density). The choice of the approach for processing experimental data is largely defined by the information that is initially available about the electrode surface and by the final information that one intends to obtain from the processed data. If the A_{ES} can be accurately measured (i.e. by an electrochemical method), the direct approach is more suitable. However, because there is not a true separation of the mass transport and inactive area effects during this processing method, the effect of θ cannot clearly be observed by following this treatment unless experiments are carefully designed in which the kinetic effects are kept the same. On the other hand, in many cases it is possible to know the fraction of active area, or the surface density of active sites of the electrode, either by using spectroscopic [118] or scanning probe techniques [119], or because the electrode was prepared using a well-defined nanostructured template [120]. In these cases, the two-step approach is

more appropriate since it allows one, in addition to obtaining information about the intrinsic activity of a material, to analyze the influence of the inactive area on the apparent activity of the material free of mass transport effects.

High mass-transport rates can also be achieved through the enhanced diffusion possible at UMEs. In this case, in the absence of convection, the inverse relationship in Eq. (10) would contain terms relating to $i(E)$, $i_{L,NP}$, and $i_K(E)$. At such electrodes, much smaller dispersions of NPs can be considered and techniques such as scanning electrochemical microscopy (SECM) can be used to investigate the attached NPs. Such investigations are ongoing in these laboratories and other laboratories. For example, electrocatalysis has been reported at UMEs with a single attached NP [28], with dispersed catalysts [121], and through NP collisions at a UME surface [105,122,123].

Acknowledgement

We appreciate valuable discussions with Dr. A.J. Bard. The financial support of the National Science Foundation (Grants CHE-0210315, CHE-0809966, EPS-0447691/NMSU Costshare, and ADVANCE-0123690 to C.G.Z.) is gratefully acknowledged. Partial support from a NMSU GREG award (to C.G.Z. and D.G.) is gratefully acknowledged. JLF thanks Universidad Nacional del Litoral and CONICET (Argentina) for travel expense support.

References

[1] S. Gottesfeld, T.A. Zawodzinski, in: R.C. Alkire, H. Gerischer, D.M. Kolb, C.W. Tobias (Eds.), Advances in Electrochemical Science and Engineering, vol. 5, Wiley-Interscience-VCH, Weinheim, 1997, p. 195.
[2] L. Carrete, K.A. Friedrich, U. Stimmming, Fuel Cells 1 (2001) 5–39.
[3] J.M. Feliu, E. Herrero, Handbook of Fuel Cells: Fundamentals, Technology, and Applications, Wiley and Sons, Ltd., Chichester, 2003.
[4] K.F. Blurton, P. Greenberg, H.G. Oswin, D.R. Rutt, J. Electrochem. Soc. 119 (1972) 559–564.
[5] L.J. Bregoli, Electrochim. Acta 23 (1978) 489–492.
[6] M. Peukcert, T. Yoneda, R.A.D. Betta, M. Boudart, J. Electrochem. Soc. 133 (1986) 944–947.
[7] S. Mukerjee, J. Appl. Electrochem. 20 (1990) 537–548.
[8] S.L. Gojkovic, S.K. Zecevic, R.F. Savinell, J. Electrochem. Soc. 145 (1998) 3713–3720.
[9] M. Watanabe, S. Saegusa, P. Stonehart, Chem. Lett. (1988) 1487–1490.
[10] M. Watanabe, H. Sei, P. Stonehart, J. Electroanal. Chem. 261 (1989) 375–387.
[11] N. Giordano, E. Passalacqua, L. Ping, A.S. Arico, V. Antonucci, M. Vivaldi, K. Kinoshita, Electrochim. Acta 36 (1991) 1979–1984.
[12] K. Kinoshita, J. Electrochem. Soc. 137 (1990) 845–848.
[13] K. Kinoshita, in: J.O'M. Bockris, B.E. Conway, R.E. White (Eds.), Modern Aspects of Electrochemistry, vol. 14, Plenum Press, New York and London, 1982, pp. 557–637.
[14] K. Kinoshita, P. Stonehart, in: J.O'M. Bockris, B.E. Conway (Eds.), Modern Aspects of Electrochemistry, vol. 12, Plenum Press, New York and London, 1977, pp. 183–266.
[15] E. Higuchi, H. Uchida, M. Watanabe, J. Electroanal. Chem. 583 (2005) 69–76.
[16] K.J.J. Mayrhofer, B.B. Blizanac, M. Arenz, V.R. Stamenkovic, P.N. Ross, N.M. Markovic, J. Phys. Chem. B 109 (2005) 14433–14440.
[17] H. Yano, J. Inukai, H. Uchida, M. Watanabe, P.K. Babu, T. Kobayashi, J.H. Chung, E. Oldfield, A. Wieckowski, Phys. Chem. Chem. Phys. 8 (2006) 4932–4939.
[18] S. Kumar, S. Zou, Langmuir 25 (2009) 574–581.
[19] V. Komanicky, H. Iddir, K.C. Chang, A. Menzel, G. Karapetrov, D. Hennessy, P. Zapol, H. You, J. Am. Chem. Soc. 131 (2009) 5732.
[20] D. Tripkovic, S. Stevanovic, A. Tripkovic, A. Kowal, V.M. Jovanovic, J. Electrochem. Soc. 155 (2008) B281.
[21] A. Damjanovic, M.A. Genshaw, J.O.M. Bockris, J. Electrochem. Soc. 114 (1967) 466.
[22] A. Damjanovic, M.A. Genshaw, J.O.M. Bockris, J. Electrochem. Soc. 114 (1967) 1067.
[23] P.N. Ross, J. Electrochem. Soc. 126 (1979) 67–77.
[24] N.M. Markovic, R.R. Adzic, B.D. Cahan, E.B. Yeager, J. Electroanal. Chem. 377 (1994) 249–259.
[25] N.M. Markovic, H.A. Gasteiger, P.N. Ross, J. Phys. Chem. 99 (1995) 3411–3415.
[26] M.D. Macia, J.M. Campina, E. Herrero, J.M. Feliu, J. Electroanal. Chem. 564 (2004) 141–150.
[27] A. Kuzume, E. Herrero, J.M. Feliu, J. Electroanal. Chem. 599 (1997) 333–343.
[28] S. Chen, A. Kucernak, J. Phys. Chem. B 108 (2004) 3262–3276.
[29] O. Antoine, Y. Bultel, R. Durand, J. Electroanal. Chem. 499 (2001) 85–94.
[30] U.A. Paulus, T.J. Schmidt, H.A. Gasteiger, R.J. Behm, J. Electroanal. Chem. 495 (2001) 134–145.
[31] Y. Mo, S. Sarangapani, A. Le, D.A. Scherson, J. Electroanal. Chem. 538–539 (2002) 35–38.
[32] S. Kumar, S. Zou, Electrochem. Commun. 8 (2006) 1151–1157.
[33] H. Ye, R.W.J. Scott, R.M. Crooks, Langmuir 20 (2004) 2915–2920.
[34] Z.G. Estephan, L. Alawieh, L.I. Halaoui, J. Phys. Chem. C 111 (2007) 8060–8068.
[35] H. Ye, J.A. Crooks, R.M. Crooks, Langmuir 23 (2007) 11901.
[36] S. Brimaud, S. Pronier, C. Coutanceau, J.M. Leger, Electrochem. Commun. 10 (2008) 1703.
[37] T.F. Jaramillo, S.H. Baeck, B.R. Cuenya, E.W. McFarland, J. Am. Chem. Soc. 125 (2003) 7148.
[38] B.R. Cuenya, S.H. Baeck, T.F. Jaramillo, E.W. McFarland, J. Am. Chem. Soc. 125 (2003) 12928.
[39] S. Kumar, S. Zou, Langmuir 25 (2009) 574.
[40] B. Viswanath, S. Patra, N. Munichandraiah, N. Ravishankar, Langmuir 25 (2009) 3115.
[41] Y. Gu, J. St-Pierre, A. Joly, R. Goeke, A. Datye, P. Atanassov, J. Electrochem. Soc. 156 (2009) B485–B492.
[42] B.R. Cuenya, J.R. Croy, S. Mostafa, F. Behafarid, L. Li, Z. Zhang, J.C. Yang, Q. Wang, A.I. Frenkel, J. Am. Chem. Soc. 132 (2010) 8747–8756.
[43] J. Solla-Gullon, F.J. Vidal-Iglesias, P. Rodriguez, E. Herrero, J.M. Feliu, J. Clavilier, A. Aldaz, J. Phys. Chem. B 108 (2001) 13573–13575.
[44] J. Solla-Gullon, V. Montiel, A. Aldaz, J. Clavilier, J. Electroanal. Chem. 491 (2000) 69–77.
[45] H.H. Ingelsten, J.C. Beziat, K. Bergkvist, A. Palmqvist, M. Skoglundh, H. Qiuhong, L.K.L. Falk, K. Holmberg, Langmuir 18 (2002) 1811–1818.
[46] S. Garbarino, A. Pereira, C. Hamel, E. Irrissou, M. Chaker, D. Guay, J. Phys. Chem. C 114 (2010) 2980–2988.
[47] D. Tainoff, L. Bardotti, F. Tournus, G. Guiraud, O. Boisron, P. Melinon, J. Phys. Chem. C 112 (2008) 6842–6849.
[48] R.W. Lindstrom, Y.E. Seidel, Z. Jusys, M. Gustavsson, B. Wickman, B. Kasemo, R.J. Behm, J. Electroanal. Chem. 644 (2010) 90–102.
[49] A.J. Bard, L.R. Faulkner, Electrochemical Methods, Wiley, New York, 2001 (Chapter 9).
[50] K.J.J. Mayrhofer, D. Strmcnik, B.B. Blizanac, V. Stamenkovic, M. Arenz, N.M. Markovic, Electrochim. Acta 53 (2008) 3181–3188.
[51] Y.-H. Shih, G.V. Sagar, S.D. Lin, J. Phys. Chem. C 112 (2008) 123–130.
[52] S.K. Zecevic, J.S. Wainright, M.H. Litt, S.Lj. Gojkovic, R.F. Savinell, J. Electrochem. Soc. 144 (1997) 2973–2982.
[53] A. Merz, A.J. Bard, J. Am. Chem. Soc. 100 (1978) 3222–3223.
[54] P.J. Peerce, A.J. Bard, J. Electroanal. Chem. 112 (1980) 97–115.
[55] J. Leddy, A.J. Bard, J. Electroanal. Chem. 153 (1983) 223–242.
[56] D.A. Gough, J.K. Leypoldt, Anal. Chem. 51 (1979) 439–444.
[57] D.A. Gough, J.K. Leypoldt, Anal. Chem. 52 (1980) 1126–1130.
[58] D.A. Gough, J.K. Leypoldt, J. Electrochem. Soc. 127 (1980) 1278–1286.
[59] C.P. Andrieux, J.M. Saveant, in: R.W. Murray (Ed.), Molecular Design of Electrode Surfaces, Wiley and Sons, Inc., New York, 1992, pp. 207–270.
[60] J.M. Saveant, J. Electroanal. Chem. 302 (1991) 91–101.
[61] A.J. Bard, Integrated Chemical Systems: A Chemical Approach to Nanotechnology, Wiley, New York, 1994. pp. 196–205.
[62] A.J. Bard, L.R. Faulkner, Electrochemical Methods, Wiley, New York, 2001. pp. 619–623 (Chapter 14).
[63] B. Baret, P.H. Aubert, M.M. L'Hermite, M. Pinault, C. Reynaud, A. Etcheberry, H. Perez, Electrochim. Acta 54 (2009) 5421–5430.
[64] C. Amatore, J.M. Saveant, D. Tessier, J. Electroanal. Chem. 147 (1983) 39–51.
[65] K.B. Holt, A.J. Bard, Y. Show, G.M. Swain, J. Phys. Chem. B 108 (2004) 15117–15127.
[66] B.A. Brookes, T.J. Davies, A.C. Fisher, R.G. Evans, S.J. Wilkins, K. Yunus, J.D. Wadhawan, R.G. Compton, J. Phys. Chem. C 107 (2003) 1616–1627.
[67] H. Reller, E. Kirowa-Eisner, E. Gileadi, J. Electroanal. Chem. 161 (1984) 247–268.
[68] E. Gileadi, Electrode Kinetics for Chemists, Chemical Engineers, and Materials Scientists, VCH, New York, 1993. pp. 448–454.
[69] B.R. Scharifker, J. Electroanal. Chem. 240 (1988) 61–76.
[70] T.J. Davies, R.G. Compton, J. Electroanal. Chem. 585 (2005) 63–82.
[71] H.J. Lee, C. Beriet, R. Ferrigno, H.H. Girault, J. Electroanal. Chem. 502 (2001) 138–145.
[72] T.J. Davies, C.E. Banks, R.G. Compton, J. Solid State Electrochem. 9 (2005) 797–808.
[73] T.J. Davies, S.W. Jones, C.E. Banks, J. del Campo, R. Mas, F.X. Munoz, R.G. Compton, J. Electroanal. Chem. 585 (2005) 51–62.
[74] O. Ordeig, C.E. Banks, T.J. Davies, J. del Campo, F.X. Munoz, R.G. Compton, J. Electroanal. Chem. 592 (2005) 126–130.
[75] I. Streeter, R. Baron, R.G. Compton, J. Phys. Chem. C 111 (2007) 17008–17014.
[76] S.R. Belding, E.J.F. Dickinson, R.G. Compton, J. Phys. Chem. C 113 (2009) 11149–11156.
[77] S.R. Belding, R.G. Compton, J. Phys. Chem. C 114 (2010) 8309–8319.
[78] D. Ganguli, M. Ganguli, Inorganic Particle Synthesis via Macro- and Microemulsions: A Micrometer to Nanometer Landscape, Kluwer Academic/Plenum Publishers, New York, 2003.
[79] M.P. Pileni, Structure and Reactivity in Reverse Micelles, Elsevier, Amsterdam, 1989.
[80] M.A. Lopez-Quintela, J. Rivas, J. Colloid Interface Sci. 158 (1993) 446–451.
[81] H.H. Ingelsten, R. Bagwe, A. Palmqvist, M. Skoglundh, C. Svanberg, K. Holmberg, D.O. Shah, J. Colloid Interface Sci. 241 (2001) 104–111.

[82] U. Natarajan, K. Handique, A. Mehra, J.R. Rellare, K. Khilar, Langmuir 12 (1996) 2670–2678.
[83] M. Boutonnet, J. Kizling, P. Stenius, Colloid Surf. 5 (1982) 209–225.
[84] B. Niemann, P. Veit, K. Sundmacher, Langmuir 24 (2008) 4320–4328.
[85] M.P. Pileni, J. Phys. Chem. C 111 (2007) 9019–9038.
[86] M.P. Pileni, J. Exp. Nanosci. 1 (2006) 13–27.
[87] M.P. Pileni, J. Phys. Chem. 97 (1993) 6961–6973.
[88] M. Wu, D. Chen, T. Huang, Langmuir 17 (2001) 3877.
[89] J. Solla-Gullon, A. Rodes, V. Montiel, A. Aldaz, J. Clavilier, J. Electroanal. Chem. 554–555 (2003) 273–284.
[90] R.P. Bagwe, K.C. Khilar, Langmuir 16 (2000) 905.
[91] J. Solla-Gullon, V. Montiel, A. Aldaz, J. Clavilier, J. Electrochem. Soc. 150 (2003) E104–E109.
[92] V. Raghuveer, P.J. Ferreira, A. Manthiram, Electrochem. Commun. 8 (2006) 807–814.
[93] Y. Qian, W. Wen, P.A. Adcock, Z. Jiang, N. Hakim, M.S. Saha, S. Mukerjee, J. Phys. Chem. C 112 (2008) 1146–1157.
[94] S. Santra, N. Tapec, N. Theodoropoulou, J. Dobson, A. Hebard, W. Tan, Langmuir 17 (2001) 2900.
[95] C. Lu, P. Yeh, J. Mater. Chem. 10 (2000) 599.
[96] D.W. Kim, S.G. Oh, J.D. Lee, Langmuir 15 (1999) 1599.
[97] M. Antonietti, R. Basten, S. Lohmann, Macromol. Chem. Phys. 196 (1995) 441.
[98] R.P. Bagwe, K.C. Khilar, Langmuir 13 (1997) 6432–6438.
[99] R. Hilfiker, H.F. Eicke, H. Hammerich, Helv. Chim. Acta 70 (1987) 1531–1536.
[100] G.J.M. Koper, W.F.C. Sager, J. Smeets, D. Bedeaux, J. Phys. Chem. 99 (1995) 13291–13300.
[101] K. Wikander, C. Petit, K. Holmberg, M.P. Pileni, Langmuir 22 (2006) 4863–4868.
[102] R. Wood, in: A.J. Bard (Ed.), Electroanalytical Chemistry, vol. 9, Marcel Dekker, Inc., New York, 1976.
[103] C.G. Zoski, N. Yang, P. He, L. Berdondini, M. Koudelka-Hep, Anal. Chem. 79 (2007) 1474–1484.
[104] P.A. Bobbert, M.M. Wind, J. Vlieger, J. Phys. 141A (1987) 58–72.
[105] X. Xiao, A.J. Bard, J. Am. Chem. Soc. 129 (2007) 9610–9612.
[106] C.L. Colyer, D. Luscombe, K.B. Oldham, J. Electroanal. Chem. 283 (1990) 379–387.
[107] A.J. Bard, L.R. Faulkner, Electrochemical Methods, Wiley, New York, 2001. pp. 29–31, 176.
[108] A.J. Bard, L.R. Faulkner, Electrochemical Methods, Wiley, New York, 2001 (Chapter 5).
[109] A.J. Bard, L.R. Faulkner, Electrochemical Methods, Wiley, New York, 2001 (Chapter 6).
[110] S. Gottesfeld, I.D. Raistrick, S. Srinivasan, J. Electrochem. Soc. 134 (1987) 1455.
[111] A. Damjanovic, G. Hudson, J. Electrochem. Soc. 135 (1988) 269.
[112] C.G. Zoski, in: P. Vanysek (Ed.), Modern Techniques in Electroanalysis, Wiley and Sons, Inc., New York, 1996, pp. 241–312.
[113] A.M. Bond, K.B. Oldham, C.G. Zoski, Anal. Chim. Acta 216 (1989) 177–230.
[114] K.B. Oldham, J.C. Myland, C.G. Zoski, A.M. Bond, J. Electroanal. Chem. 270 (1989) 79–101.
[115] A.J. Bard, M.V. Mirkin (Eds.), Scanning Electrochemical Microscopy, Dekker, Inc., New York, Basel, 2001.
[116] J. Zhou, Y. Zu, A.J. Bard, J. Electroanal. Chem. 491 (2000) 22–29.
[117] M.V. Mirkin, T.C. Richards, A.J. Bard, J. Phys. Chem. 97 (1993) 7672–7677.
[118] S. Guerin, B.E. Hayden, D. Pletcher, M.E. Rendall, J.-P. Suchsland, J. Comb. Chem. 8 (2006) 679–686.
[119] F. Forouzan, A.J. Bard, M.V. Mirkin, Israel J. Chem. 37 (1997) 155–163.
[120] C.R. Martin, Acc. Chem. Res. 28 (1995) 61–68.
[121] D. Strmcnik, N. Hodnik, S.B. Hocevar, D. van der Vliet, M. Zofko, V.R. Stamenkovic, B. Pihlar, N.M. Markovic, J. Phys. Chem. C 114 (2010) 2640–2644.
[122] X.Y. Xiao, F.R.F. Fan, J.P. Zhou, A.J. Bard, J. Am. Chem. Soc. 130 (2008) 16669–16677.
[123] F.R.F. Fan, A.J. Bard, Nano. Lett. 8 (2008) 1746–1749.